

Quantum-enhanced photoprotection in neuroprotein architectures emerges from collective light-matter interactions

Hamza Patwa¹, Nathan S. Babcock¹, and Philip Kurian^{1,*}

¹Quantum Biology Laboratory, Howard University, Washington, D.C. 20060, USA
<https://www.quantumbiolab.com>

*E-mail: pkurian@howard.edu

Abstract

Background: Superradiance is the phenomenon of many identical quantum systems absorbing and/or emitting photons collectively at a higher rate than any one system can individually. This phenomenon has been studied analytically in idealized distributions of electronic two-level systems (TLSs), each with a ground and excited state, as well as numerically in realistic photosynthetic nanotubes and cytoskeletal architectures. **Methods:** Superradiant effects are studied here in realistic biological mega-networks of tryptophan (Trp) molecules, which are strongly fluorescent amino acids found in many proteins. Each Trp molecule acts as a chromophore absorbing in the ultraviolet spectrum and can be treated approximately as a TLS, with its $1L_a$ excited singlet state; thus, organized Trp networks can exhibit superradiance. Such networks are found, for example, in microtubules, actin filaments, and amyloid fibrils. Microtubules and actin filaments are spiral-cylindrical protein polymers that play significant biological roles as primary constituents of the eukaryotic cytoskeleton, while amyloid fibrils have been targeted in a variety of neurodegenerative diseases. We treat these proteinaceous Trp networks as open quantum systems, using a non-Hermitian Hamiltonian to describe interactions of the chromophore network with the electromagnetic field. We numerically diagonalize the Hamiltonian to obtain its complex eigenvalues, where the real part is the collective energy and the imaginary part is its associated enhancement rate. **Results:** We obtained the energies and enhancement rates for realistic microtubules, actin filament bundles, and amyloid fibrils of differing lengths, and we used these values to calculate the fluorescence quantum yield, which is the ratio of the number of photons emitted to the number of photons absorbed. We find that all three of these structures exhibit highly superradiant states near the low-energy portion of the spectrum, which enhances the magnitude and robustness of the quantum yield even in the presence of static disorder and thermal noise. **Conclusions:** The high quantum yield and stable superradiant states in these biological architectures may play a photoprotective role *in vivo*, downconverting highly energetic ultraviolet photons emitted from reactive free radical species and thereby mitigating

biochemical stress and photophysical damage. Contrary to conventional assumptions that quantum effects cannot survive in large biosystems at high temperatures, our results suggest that macropolymeric collectives of TLSs in microtubules, actin filaments, and amyloid fibrils exhibit increasingly observable and robust effects with increasing length, at least up to the micron scale, due to quantum coherent interactions in the single-photon limit. Superradiant enhancement and high quantum yield exhibited in neuroprotein polymers could thus play a crucial role in information processing in the brain, the development of neurodegenerative diseases such as Alzheimer’s and related dementias, and a wide array of other pathologies characterized by anomalous protein aggregates.

1 Introduction

Superradiance is a quantum coherent phenomenon first explored in detail by Robert Dicke [1] in 1954. Superradiance arises from the interaction of a collective of quantum systems with the external electromagnetic field. Thus, the theoretical formalism that describes superradiance is given frequently in the language of open quantum systems. In collectives of quantum systems with discrete energy levels, collective superradiant states are characterized by the collective decay rate Γ of the system being much larger than the single-system decay rate γ . An eigenstate with a larger decay is more short-lived than an eigenstate with a small decay rate. In other words, an absorbed photon in an eigenstate with a larger decay rate will be very quickly re-emitted into the environment. The reason that the decay rate is larger for a collective of quantum systems than one system is that in a collective, the excitation is delocalized across the collective, rather than being incoherently concentrated on a single system.

Superradiant effects in the ultraviolet region of the electromagnetic spectrum have been studied for biosystems [2–4] and emerge largely due to collective light-matter interactions involving tryptophan (Trp), which is a strongly fluorescent amino acid found in many proteins. It has many notable photophysical properties, such as its strong ultraviolet absorption, significant absorption-emission Stokes shift, and large transition dipole moment. Trp can be modeled as a two-level system (TLS), which has a ground and an excited state [5]. Other amino acids such as tyrosine, phenylalanine, and cysteine also absorb in the ultraviolet, but much more weakly than Trp. The fact that Trp networks absorb in the ultraviolet means that the excitation wavelengths are frequently shorter than the characteristic length scales of the biological scaffolds in which such networks lie ($\lambda \lesssim L$), a sharp distinction from the longer visible wavelengths that excite smaller photosynthetic light-harvesting complexes. This implies that long-range interactions in the ultraviolet-excited system will play a more prominent role in the light-matter dynamics.

Coherent quantum phenomena arising from organized networks of chromophores in protein scaffolds have been shown to play a role in the efficiency of photosynthetic complexes [6–10] and of other light-harvesting structures (see [2, 11–14] and references therein). More recently, superradiant states have been experimentally confirmed in tryptophan net-

works of microtubules (MTs) and theoretically predicted in centrioles¹ and neuronal axon bundles [3]. In this work, we study the role of superradiance in a wider class of neuroprotein polymers, including cytoskeletal filaments and pathological aggregates, thereby demonstrating the generalizability of our prior experimental results and theoretical predictions for a novel group of chromophore architectures with significant implications for a host of neurodegenerative and other complex diseases.

2 Background

2.1 Cytoskeleton: Microtubules and Actin Filaments

The cytoskeleton is a dynamic structure in eukaryotic cells that provides structural support and acts as a transport mechanism for molecules inside the cell. It has three main components: microtubules, actin filaments, and intermediate filaments. In this work, we specifically focus on microtubules and actin filaments.

Microtubules (pictured in Fig. 1(A)), spiral-cylindrical structures made of tubulin dimers, play a role in cell communication and mitosis. They are a dynamic part of the cytoskeleton, being able to quickly grow and shrink via polymerization or depolymerization, respectively. Microtubules also make up the internal structure of external appendages such as flagella and cilia, which are important for locomotion and movement. Intra-cell communication is also facilitated by microtubules, as well as the whole cytoskeleton in general. Microtubules are a primary constituent of axons in the brain. They have been shown to play an important role in transport along axonal processes in neurons [23], so disruption of microtubule transport processes in neurons has been linked to several neurodegenerative diseases.

Actin filaments (pictured in Fig. 1(B)) are strandlike structures that play an important role in the cytoskeleton. Within the context of the cytoskeleton, they are known as microfilaments, reflecting their small diameter generally less than one-third that of microtubules (see Fig. 1 for comparison). Actin filaments can bundle together to form hexagonal arrangements [24], which we also analyze in this work. They provide contractile and protrusive forces to stabilize the cytoskeleton and assist with the mobility of the cell. Like microtubules, they assist in transport from outside the cell to the inside. Actin also plays a role in the contractile apparatus of muscle cells, in the form of so-called thin filaments, and helps to maintain the structure of dendritic spines, tiny protrusions from dendrites that form functional contacts with neighboring axons of other neurons in the brain. Dendritic spines play a significant role in plasticity and processing of memory. Therefore, the role of actin has been investigated in synaptic failure in neurodegenerative diseases such as Alzheimer’s [25].

¹Centrioles are cylindrically symmetric organelles formed from nine triplets of microtubules exhibiting a pinwheel-like structure (see [15] for more specifics on their geometry). They are highly conserved in most eukaryotic cells, but notably absent in yeast and higher plants, among others [15]. Centrioles play an important role in forming the spindle complex in cell division, where they help ensure that the correct number of chromosomes are present in each daughter cell after replication [16, 17]. They have also been shown, in several studies by Guenter Albrecht-Buehler [18–21], to aid orientation of the cell to an external light stimulus.

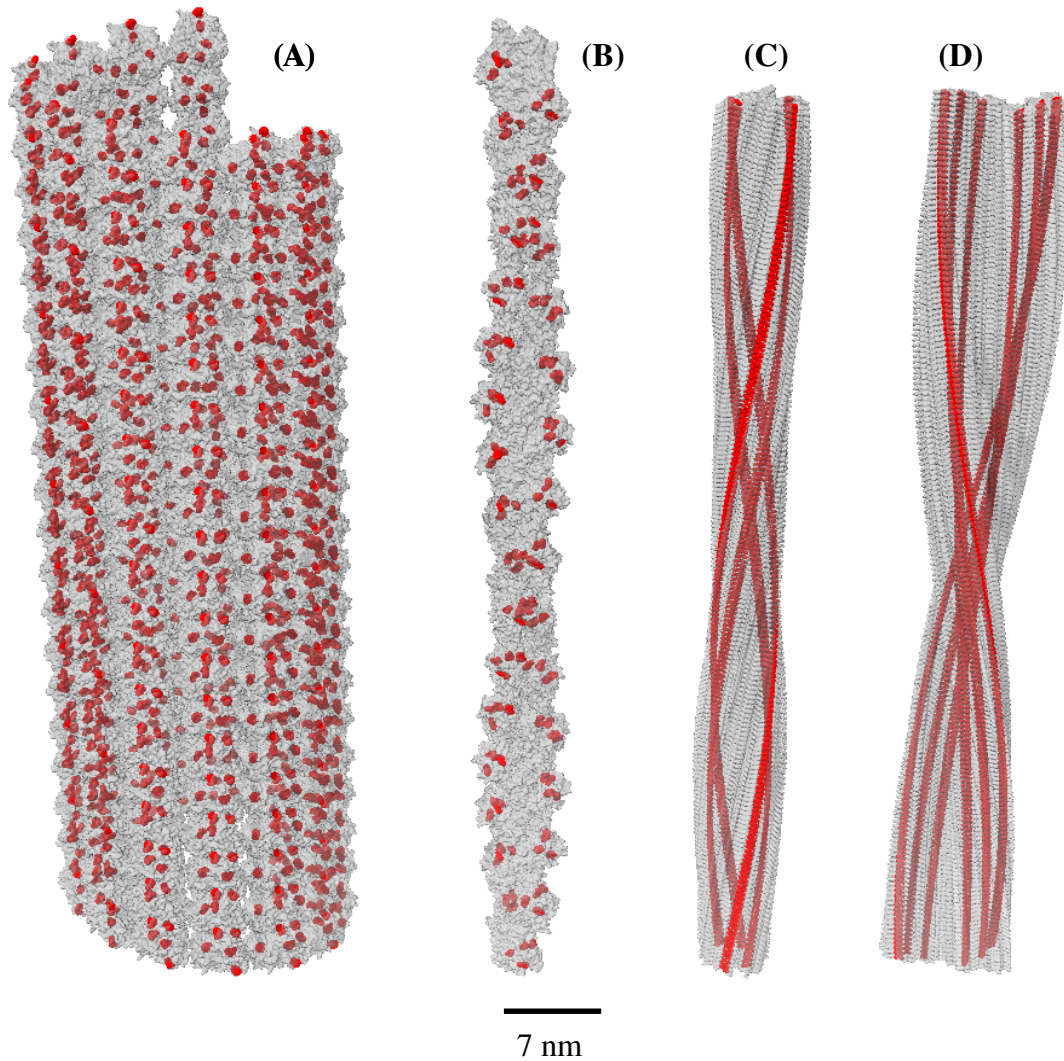


Figure 1: Tryptophan (Trp) network geometries in a model **(A)** 80-nm microtubule (built from tubulin dimer PDB entry 1JFF), **(B)** 90-nm actin filament (built from actin subunit PDB entry 6BNO), **(C)** 86.4-nm human amyloid fibril (built from amyloid subunit PDB entry 6MST), and **(D)** 86.4-nm mouse amyloid fibril (built from amyloid subunit PDB entry 6DSO). The Trp molecules are colored in red and have been enlarged for ease of viewing, within each gray protein lattice. Scale bar is valid for the entire figure.

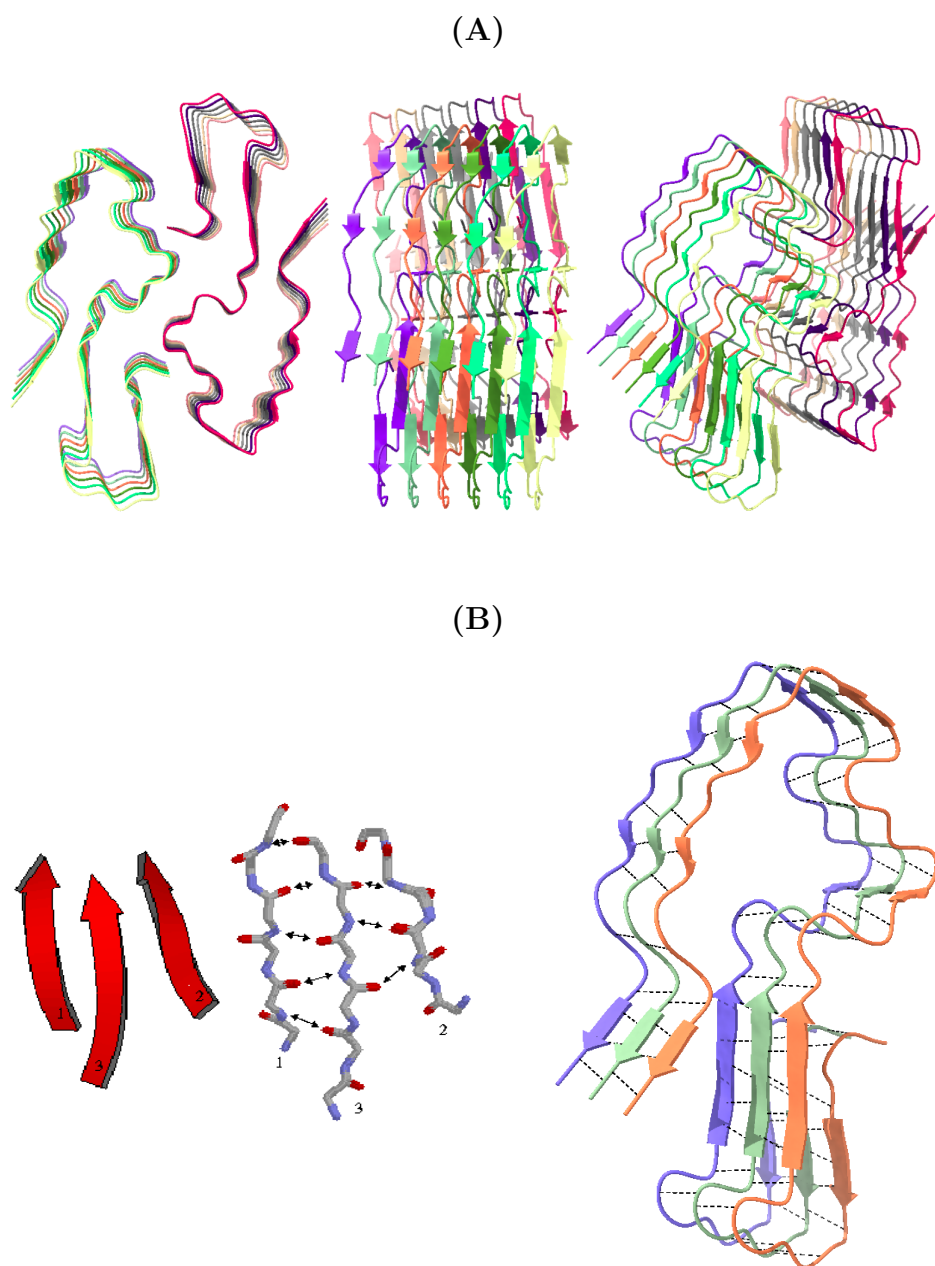


Figure 2: Structure of a single human amyloid subunit and its distinctive parallel β -sheet structure. (A) The structure of a human amyloid subunit (PDB entry 6MST) in cartoon/ribbon from a top-down view (left), side-on view (middle), and angled view (right). (B) Visual of parallel β -sheet structure of the human amyloid subunit. The left image is the structure of a parallel β -sheet, reproduced from [22]. The right image is three chains from a human amyloid subunit with the hydrogen bonds highlighted in black dashes, showing the similarity with the left image.

2.2 Pathological Aggregates: Amyloid Fibrils

Amyloid fibrils (Figs. 1(C) and 1(D)) are helical aggregates of amyloid proteins. Amyloids, the building blocks of amyloid fibrils, are a class of self-assembling proteins that fold in a β -sheet structure. The β -sheet structure, originally discovered by Herman Branson, Linus Pauling, and collaborators [26], consists of so-called β -strands, each of which forms a zig-zag pattern, and which are connected laterally to each other via hydrogen bonding to form a pleated sheet. The β -sheet has a twist (i.e., the zig-zag sheet is not confined to undulations in a single plane). Multiple β -sheets stacked on top of one another form amyloid fibrils, which are also called β -helices. An image of a human amyloid subunit (PDB entry 6MST) is pictured in Fig. 2(A). In Fig. 2(B), we can see how a human amyloid subunit forms a β -sheet structure. Typical amyloid fibrils can grow up to several micrometers in length [27–29]. Many different proteins can form amyloids, such as amyloid-beta ($A\beta$) [30], islet amyloid polypeptide (IAPP) [31], lysozyme [32], and insulin [33], and they are all associated with different pathological diseases. $A\beta$ is associated with Alzheimer’s disease, while IAPP, lysozyme, and insulin are associated with type II diabetes, lysozyme amyloidosis, and injection-localized amyloidosis, respectively [34]. There are three main models that were proposed for how amyloids are created from the original protein fold: the refolding, natively disordered, and gain-of-interaction models [35]. The most well-known of these is the refolding model, in which the protein folds from its native state to an amyloid state. Through such a mechanism, amyloids form amyloid fibrils, which can further aggregate and form clumps known as amyloid plaques. Amyloid, amyloid fibrils, and amyloid plaques are a hallmark of neurodegenerative diseases, such as Alzheimer’s and related dementias.

Another indicator of Alzheimer’s disease is the formation of neurofibrillary tangles, abnormal aggregates of the tau protein. The tau protein aids in structural support of microtubules in the brain [36], which start to disintegrate in Alzheimer’s disease. The tau proteins fall off and undergo hyperphosphorylation, which causes them to transition from an unfolded state to a folded state capable of aggregating into threadlike structures inside neurons, called tangles [37]. Tangles block transport and inhibit communication between neurons. The population density of tangles is strongly linked to the severity of cognitive decline in Alzheimer’s disease [37, 38].

2.3 Toy models of cylindrical geometries of ultraviolet-excited transition dipoles

First, we present a preliminary analysis of some toy models, in order to gain physical intuition and insight on how transition dipole vector orientations affect the photophysical properties of prototypical biological structures with cylindrical symmetry. We consider two idealized architectures of molecules based on the ones studied in [39]. Each molecule has the photophysical parameters of Trp (excitation wavelength of 280 nm and decay rate of $\sim 2.73 \times 10^{-3} \text{ cm}^{-1}$), but different transition dipole geometries. The architectures consist of multiple rings parallel to the x - y plane, each stacked on top of one another and separated by a distance L in the z -direction. The first dipole vector arrangement is the case in which all vectors point in the $+z$ direction. We call this the parallel dipole (PD) arrangement. The next arrangement is where the dipoles are all pointing in the x - y plane tangent to the ring,

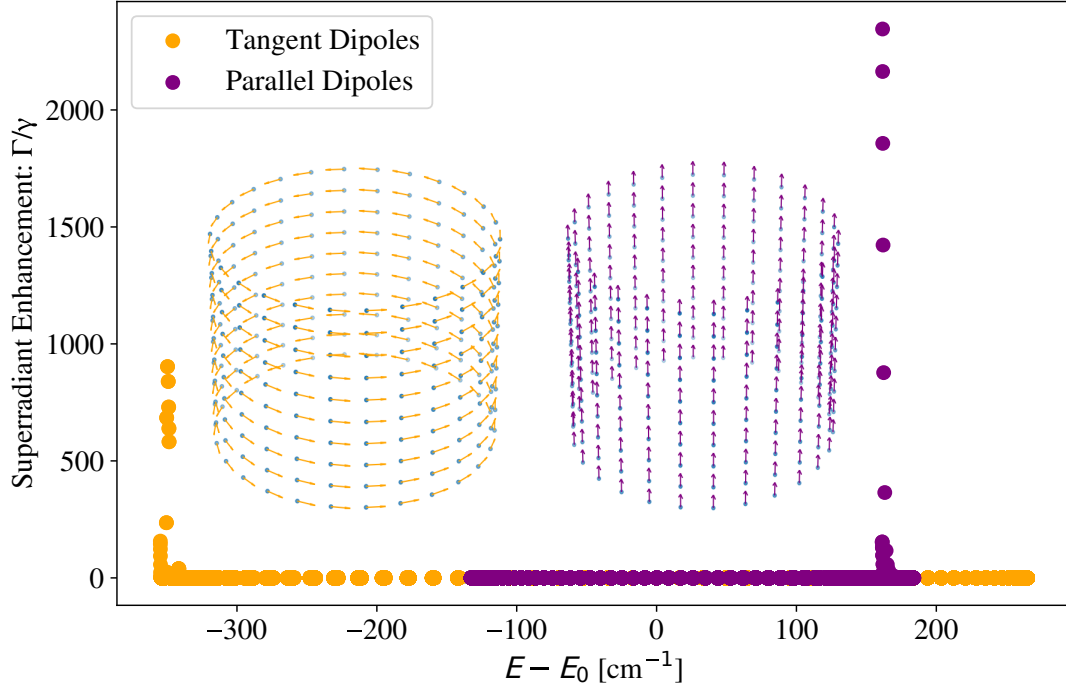


Figure 3: Plot of the eigenvalue spectrum (superradiant enhancement rate vs. energy) of idealized ring structures, with the transition dipole vectors of each cylinder plotted inset in their corresponding colors. Each transition dipole has the photophysical parameters of a tryptophan (Trp) chromophore: an excitation wavelength of 280 nm and a fluorescent decay rate of $\sim 2.73 \times 10^{-3} \text{ cm}^{-1}$. Each ring has a diameter of 22.4 nm, corresponding to the inner diameter of a microtubule. We see that, for these idealized structures, the superradiant states arise at only a very few specific energies.

the so-called tangent dipole (TD) arrangement. See the insets from Fig. 3 for a visual representation of the structures. We solve for the the eigenstates of the PD and TD arrangements under the effective Hamiltonian (1).

Fig. 3 shows the eigenspectrum of the TD and PD arrangements. An interesting feature of the spectrum is that both the TD and PD structures have superradiant states at a few specific energies, rather than being distributed across many energies. This feature arises from a specific property of the transition dipole vector arrangements: each vector’s orientation is only slightly deformed from its nearest neighbors (or, in the case of the PD arrangement, not modified at all). This symmetrical geometry of the transition dipole vectors creates a selection for a very small range of energies that contain superradiant states.

The spectrum having this unique property is significant because it influences the quantum yield (QY), defined as the ratio of the number of photons emitted to the number of photons absorbed, as well as its thermal average ($\langle \text{QY} \rangle_{th}$; see the Methods in Section 6 for more details on the quantum yield). A spectrum with the majority of superradiant states lying at the lower end of the energy spectrum will have a higher $\langle \text{QY} \rangle_{th}$, since lower energies are weighted higher in a thermal Gibbs distribution, while a spectrum with superradiant states near the high-energy portion will have a lower $\langle \text{QY} \rangle_{th}$. This means that structures that are similar to a TD structure are likely to have a higher $\langle \text{QY} \rangle_{th}$, while structures similar to PD arrangements may have a lower $\langle \text{QY} \rangle_{th}$ value. This will be discussed further in relevant biostructures, in the ensuing sections.

This analysis is different from the analysis done in [39] in significant ways. Our analysis uses the parameters for the Trp chromophore, which has an absorption peak at ~ 280 nm and a decay rate of $\sim 2.73 \times 10^{-3} \text{ cm}^{-1}$, while in [39], the photosynthetic chromophores absorb in the visible (~ 650 nm) and have a smaller decay rate of $\sim 1.821 \times 10^{-4} \text{ cm}^{-1}$. The physics changes in a critical way when the excitation wavelength changes from the visible to the ultraviolet: the biosystem sizes considered generally become comparable to or larger than the excitation wavelength, as can be the case for characteristic microtubules, actin filaments, and amyloid fibrils in the brain. Thus, we employ a widely used effective Hamiltonian for the light-matter interactions that couples the Trp chromophores at long range due to their collective interactions with the electromagnetic field. This Hamiltonian is non-Hermitian because the large number of degrees of freedom of the electromagnetic field are traced out to give an effective description of the (collective) open quantum system, whose probability amplitude decays to the field with time. For further details on the non-Hermitian formalism, please see [40–43].

3 Results

We present the eigensolutions of the effective Hamiltonian given in Eq. (1) for microtubules, actin filaments, and amyloid fibrils of varying lengths (for details on the geometry of these structures, see the Methods in Section 6, and for a visual image, see Fig. 1). We also consider the thermal average of the quantum yield (see Section 6: Methods for further details), its dependence on system size, and its robustness to static disorder. The effective Hamiltonian is non-Hermitian, and can be written as the sum of a Hermitian part and a non-Hermitian

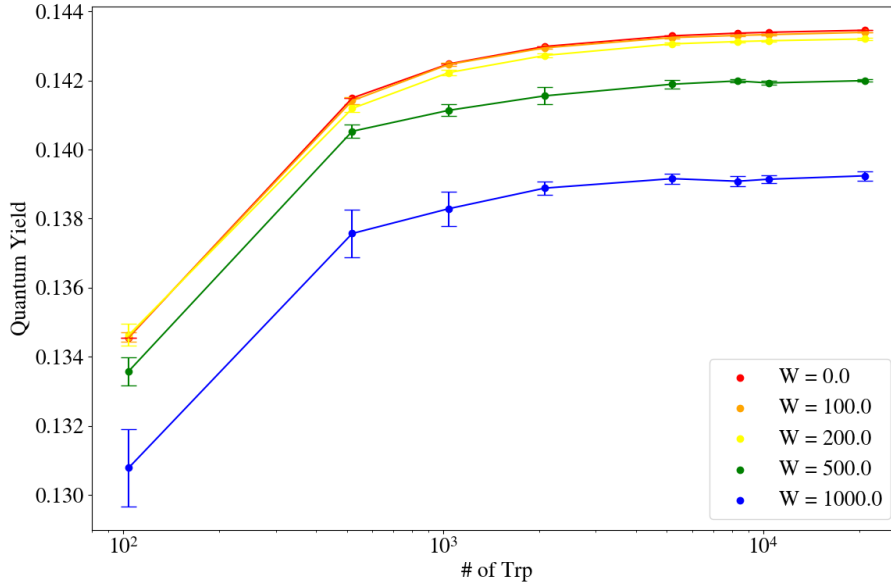


Figure 4: Thermal average of the quantum yield (QY) vs. number of tryptophan (Trp) molecules for varying static disorder strengths for single microtubules (pictured in Fig. 1(A)). W (in units of cm^{-1}) represents the strength of static disorder applied to (1), where each diagonal element of the effective Hamiltonian $H_{\text{eff},ii}$ is replaced by a random value in the range $[H_{\text{eff},ii} - W/2, H_{\text{eff},ii} + W/2]$. Then the Hamiltonian is diagonalized to find the eigenvalues, and from the eigenvalues the thermal average of the quantum yield is obtained. This is repeated ten times, and the mean is taken to obtain a data point. The error bars on each point represent one standard deviation of the ten QY values calculated for that point.

part

$$H_{\text{eff}} = H_0 + \Delta - \frac{i}{2}G, \quad (1)$$

where H_0 , Δ , and G are real matrices. Because of the non-Hermitian part $-\frac{i}{2}G$, the eigenvalues of this matrix are complex numbers. Assuming that the dimension of the matrix is N , then the (right) eigenvectors $|\mathcal{E}_j\rangle$ and their associated eigenvalues \mathcal{E}_j are

$$H_{\text{eff}}|\mathcal{E}_j\rangle = \mathcal{E}_j|\mathcal{E}_j\rangle; \quad \mathcal{E}_j = E_j - \frac{i}{2}\Gamma_j, \quad (2)$$

where E_j is the energy (real part of eigenvalue) and Γ_j is the decay rate (-2 times imaginary part of eigenvalue) of the eigenvector $|\mathcal{E}_j\rangle$. For further details, please see the Methods in Section 6.

3.1 Microtubules

We study single microtubules of varying length constructed as spiral-cylindrical collectives of tubulin dimers (PDB entry 1JFF). One tubulin dimer contains 8 Trp molecules, and one spiral of the microtubule contains 13 tubulin dimers (so one spiral contains $8 \times 13 = 104$ Trp molecules). For example, a 100-spiral microtubule contains $104 \times 100 = 10400$ Trp molecules.

Shown in Fig. 4 is the thermal average of the quantum yield (QY) as a function of the length of the microtubule, reported as the number of Trp molecules. Each color represents a differing static disorder strength, with red being the smallest ($W = 0 \text{ cm}^{-1}$) and blue being the largest ($W = 1000 \text{ cm}^{-1}$), which is approximately five times larger than static disorder in a room-temperature environment ($W = 200 \text{ cm}^{-1}$). Let us now define $\% \Delta \text{QY}(W : W_i \rightarrow W_f)$ as the percent change in quantum yield when the static disorder goes from $W_i \text{ cm}^{-1}$ to $W_f \text{ cm}^{-1}$ for a set system size. Using this notation for a system size of 20800 Trp molecules (200 spirals; the rightmost data points in Fig. 4), $\% \Delta \text{QY}(W : 0 \rightarrow 1000) = -3.08\%$. The quantum yield dampening by only 3.08% when the static disorder is five times that of room temperature demonstrates its robustness. Such quantum yield robustness to static disorder has recently been experimentally confirmed for microtubules at room temperature [3] (also see Figs. S6 and S7 of [3] for theoretical predictions of the enormous superradiant enhancements for axonal microtubule bundles, and of the quantum yield robustness for centrioles, respectively). This suggests that quantum yield robustness can be observed for similar biological structures, once realized experimentally.

The robustness of the quantum yield for microtubules (and their bundled architectures) is explainable from the shape of the spectrum of eigenvalues of the non-Hermitian Hamiltonian (1). The spectrum of single microtubules has been studied in [2]. Specifically, in Fig. 2c) of [2], the spectrum of a 100-spiral microtubule (10400 Trp molecules) is shown. It can be seen that the most superradiant states lie in the low-energy portion of the spectrum. Examining Eq. (12), if a large Γ_j is associated with a smaller E_j , then the term $\Gamma_j \exp(-\beta E_j)$ in the Gibbs thermal ensemble will be weighted more strongly, thereby augmenting the quantum yield.

In the case of microtubules, the dependence of the thermal average of the quantum yield on system size also highlights that collective light-matter interactions can enhance quantum effects beyond the length scales normally associated with quantum behavior. Let us define

$\% \Delta \text{QY}(N : N_i \rightarrow N_f)$ to be the percent change in the quantum yield at a fixed static disorder strength, when the structure goes from N_i Trp molecules to N_f Trp molecules. The QY has been determined experimentally to be 0.124 for Trp alone in BRB80 aqueous buffer solution [3]. For microtubules, when $W = 0 \text{ cm}^{-1}$, $\% \Delta \text{QY}(N : 1 \rightarrow 20800) = 15.76\%$. With a static disorder of $W = 1000 \text{ cm}^{-1}$, $\% \Delta \text{QY}(N : 1 \rightarrow 20800) = 12.31\%$. So, even with extremely large static disorder strengths, at thermal equilibrium, the quantum yield for microtubules is enhanced as the system size grows.

We also study the effects of mechanical/vibrational degrees of freedom on the superradiant states of microtubules (see Figs. S1, S2 in the Supplementary Material), within the Born-Oppenheimer approximation. As seen in these figures, the superradiance is dynamically altered by nuclear geometry and changes when microtubules are mechanically deformed in different ways. Purely longitudinal modes (only deforming along the microtubule main axis) have higher superradiance than modes with purely twisting motions around the microtubule main axis, which have higher superradiance than bending motions off the microtubule main axis. Mode 15 has purely longitudinal stretching/contracting motions, which still preserve a Γ/γ factor of greater than 27. This mode has the highest superradiance of any mode in Figs. S1 and S2. The mode with the next highest superradiance is mode 9, with a 180-degree twisting motion along the microtubule axis. Some of the large bending motions displayed in modes 12, 13, and 17 dampen the superradiance down to a Γ/γ factor of less than 10. These results show that the superradiance is modified depending on not only the biological type of structure, but its intrinsic mechanical modes. Microtubules form long, straight, packed bundles in neuronal axons, which would mostly have longitudinal stretching/contracting modes. From this analysis, we show that longitudinal vibrational modes would not dampen superradiance as much as other modes, suggesting that highly stable structures such as axons may actively be exploiting quantum coherent effects based on their architecture and which mechanical modes are allowed. Although we only conduct this analysis for microtubules, the modulation of superradiant effects with vibrational state can be extended to other structures.

The vibrational modes studied have a mechanical frequency in the low gigahertz range [44], corresponding to a timescale on the order of nanoseconds. As a microtubule oscillates mechanically, any superradiant states supported by the given atomic/nuclear configuration can vary from their enhancement factors reported in both the left and right columns of Figs. S1 and S2, to enhancement factors one or two orders of magnitude higher near the amplitude node of each vibration (see middle panels), where the structure is closest to a “straight” longitudinal configuration. From Table 1, we can see that the lifetimes for the superradiant states of microtubules and of many other structures are on the order of picoseconds. Thus, the photophysical effect of superradiance is operating on a timescale at least three orders of magnitude faster than the mechanical motion of the microtubule, which can be considered more or less static in this ultrafast regime. However, even though our predictions have all been calculated within the Born-Oppenheimer approximation, it is clear from Table 1 that the most subradiant states—and even a few of the superradiant states—supported by these neuroprotein architectures are extremely long-lived, suggesting potential influence and interaction across electronic and nuclear degrees of freedom in these structures. In many of the middle columns, we can see high exciton probabilities near the ends of the structures, despite the mode being symmetric. This could be a biological manifestation of topological edge states, which have been previously studied in paradigmatic non-Hermitian

systems [45, 46].

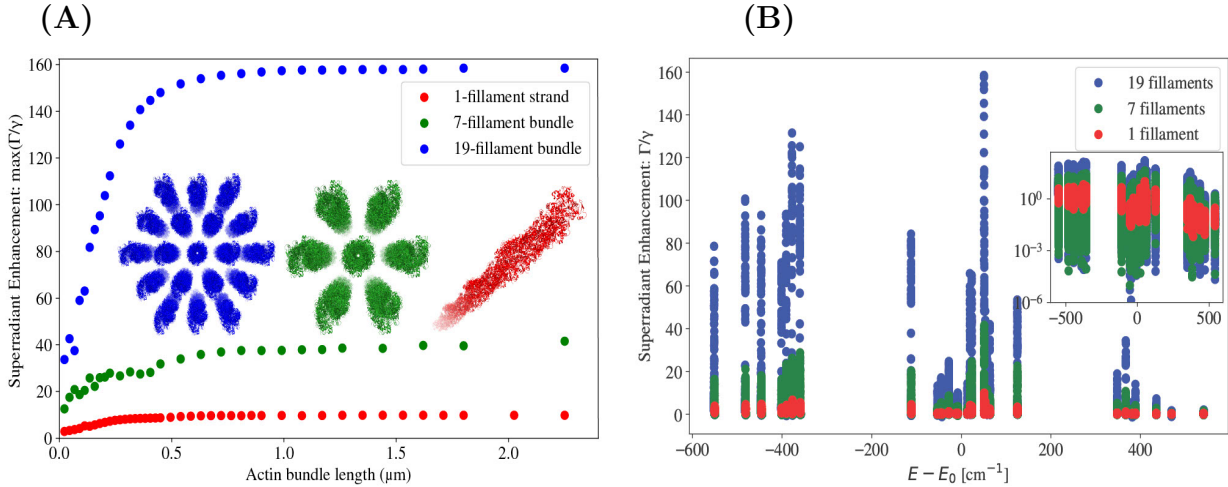


Figure 5: **(A)** Plot of the maximum superradiance $\max(\Gamma_j/\gamma)$ vs. structure length for model actin filament structures. Filaments have diameters of ~ 7 nm, and the hexagonal bundles have filaments spaced 12 nm from each other center-to-center. Sample images of 1-filament (3200 tryptophan), 7-filament (22400 tryptophan), and 19-filament (60800 tryptophan) actin structures are shown inset to the plot with their corresponding colors. **(B)** The eigenvalue spectrum (Γ_j/γ vs $E - E_0$) of 2.25- μm actin structures with 1 filament, 7 filaments, and 19 filaments in their corresponding colors. Inset is the same spectrum plotted with the y axis on a semi-log scale.

3.2 Actin filaments

We study two different types of actin collectives: actin filaments and actin bundles. An actin filament is made from a concatenation of bare actin subunits (PDB entry 6BNO), each of which is a homo-octamer (protein consisting of eight identical chains) about 22.5 nm long. We then study two sizes of actin bundles corresponding to the smallest hexagonal configurations: 7-filament bundles, and 19-filament bundles (a top-down view of both of these are pictured in the inset of Fig. 5(A)). One bare actin subunit contains 32 Trp molecules. So, for example, a 19-filament bundle comprised of single-subunit actin filaments contains $32 \times 19 = 608$ Trp molecules. Also, the Trp network in actin filaments forms a helical structure, which repeats approximately every 40 nm.

In Fig. 5, panel (A) shows the enhancement rate of the maximally superradiant state against the length of an actin filament or of a bundle of actin filaments. Similarly to the case of microtubules, the maximum superradiant enhancement rate increases with length at first, and then eventually saturates when the length approaches or exceeds the excitation wavelength. This feature is most pronounced in the 19-filament actin bundles. In the single filament and the 7-filament bundle, saturation of the maximum enhancement rate starts to occur when the length of the actin structure is around the length scale of excitation (280 nm). However, in the 19-filament bundle, saturation occurs at about twice that length. This

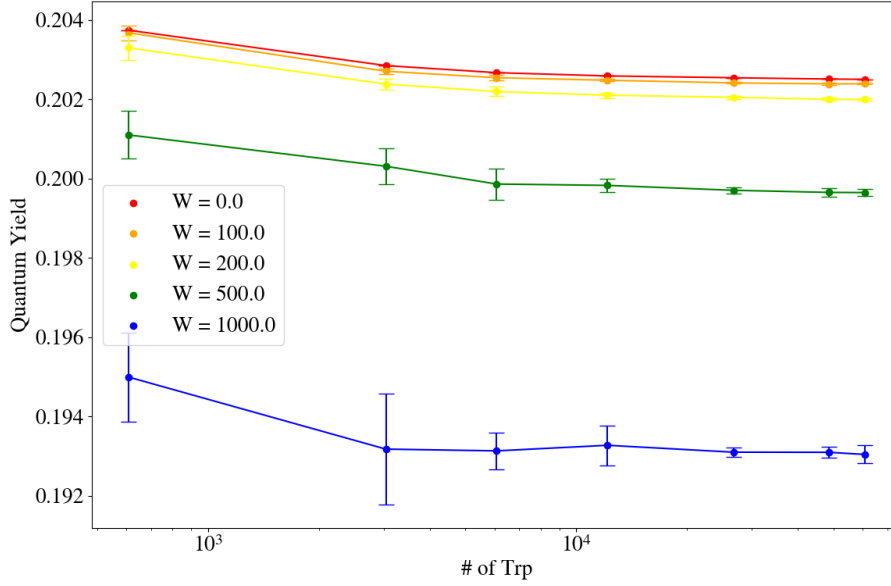


Figure 6: Thermal average of the quantum yield (QY) vs. number of tryptophan (Trp) molecules for varying static disorder strengths for 19-filament bundles of actin (one actin filament is pictured in Fig. 1(B), and a 19-filament bundle is pictured inset in blue in Fig. 5(A)). W (in units of cm^{-1}) represents the strength of static disorder applied to (1), where each diagonal element of the effective Hamiltonian $H_{\text{eff},ii}$ is replaced by a random value in the range $[H_{\text{eff},ii} - W/2, H_{\text{eff},ii} + W/2]$. Then the Hamiltonian is diagonalized to find the eigenvalues, and from the eigenvalues the thermal average of the quantum yield is obtained. This is repeated ten times, and the mean is taken to obtain a data point. The error bars on each point represent one standard deviation of the ten QY values calculated for that point.

is an interesting difference between microtubules/microtubule bundles [2, 3], which saturate in their maximum superradiant enhancement (in the single-photon limit) at about three or more times the excitation wavelength, and actin filaments/bundles.

In panel **(B)** of Fig. 5, we can see that the maximally superradiant states of 2.25 μm -long actin structures are not close to the lowest exciton state. This impacts the quantum yield of actin bundles and filaments, as seen in Fig. 6. With zero static disorder, $\% \Delta \text{QY}(N : 1 \rightarrow 60800) = 62.31\%$ and with $W = 1000 \text{ cm}^{-1}$, $\% \Delta \text{QY}(N : 1 \rightarrow 60800) = 55.14\%$. Even though the QY of actin bundles is enhanced for large structures with respect to Trp alone in solution, it can be seen in Fig. 6 that all curves show a very slight decrease in the QY. Specifically, $\% \Delta \text{QY}(N : 608 \rightarrow 60800) = -1.11\%$ for $W = 0 \text{ cm}^{-1}$. For room-temperature static disorder of $W = 200 \text{ cm}^{-1}$, such a decrease is still present, although for $W = 1000 \text{ cm}^{-1}$, the change is within the error bars of the static disorder. Despite this decrease being small, its existence means that once a 19-filament bundle of single-subunit actin filaments is created, increasing the filament length further does not enhance the QY at all, contrary to the microtubule case. For the dependence of the QY of actin bundles with static disorder, we calculated $\% \Delta \text{QY}(W : 0 \rightarrow 1000) = -4.17\%$ for a 60800-Trp actin bundle (60800 Trp = 2.25 μm). This means that, at thermal equilibrium, the QY for large actin structures is dampened only slightly more than the QY for single microtubules.

Comparing Fig. 5 to the analogous spectrum for microtubules (see Fig. 2 of [2]), and by examining the entries of Table 1, we see that microtubules have brighter superradiant states than those for all actin structures. However, 19-filament actin bundles still have higher predicted QY values (see Fig. 6) than those for microtubules (see Fig. 4). We can understand this by revisiting Eq. (12). Each decay rate Γ_j is weighted by a Boltzmann factor $\exp(-\beta E_j)$. If the energy E_j is much smaller than the single-Trp excitation energy (our “zero” reference) and has a relatively large absolute value compared to this collective Lamb shift, this can compensate for the decay rate being small. Fig. 5 shows that the lowest energy states are shifted about -600 cm^{-1} , while for microtubules the lowest energy states are shifted only about -100 cm^{-1} . This is due to the Trp-Trp interactions in actin filaments being much larger than the Trp-Trp interactions in microtubules. For a 35-spiral microtubule (280-nm length), the average Trp-Trp interaction is 0.0311 cm^{-1} , with a standard deviation of 0.898 cm^{-1} . The nearest-neighbor Trp-Trp interaction is 62.82 cm^{-1} , which is small compared to room temperature ($k_B T \approx 200 \text{ cm}^{-1}$). An actin filament of 13 subunits (292.5 nm), on the other hand, has an average Trp-Trp interaction of 0.683 cm^{-1} , with a standard deviation of 14.06 cm^{-1} . The nearest-neighbor Trp-Trp interaction for an actin filament is 537.2 cm^{-1} , much larger than room temperature. The strength of the Trp-Trp couplings in actin compared to microtubules explains the larger collective Lamb shift for lower-energy states in actin, thereby explaining its high quantum yield despite having dimmer superradiant states than microtubules.

These results show that although the absolute values of the QYs for 19-filament actin bundles are larger than that of single microtubules, these QYs for actin bundles decrease with system size after even a single twist (608 Trp). However, 19-filament actin bundles are comparable to microtubules in their QY robustness to static disorder. Although such actin bundles do exhibit observable and important superradiant effects via the QY, our results imply that their role in cytoskeletal dynamics may be restricted, more so than microtubules, to their conventional mechanical roles rather than having significant photophysical enhance-

ments at long length scales. Experiments *in vitro* to detect superradiant QY enhancements (from Trp in solution) in actin bundles would be warranted, as has been demonstrated with microtubules [3].

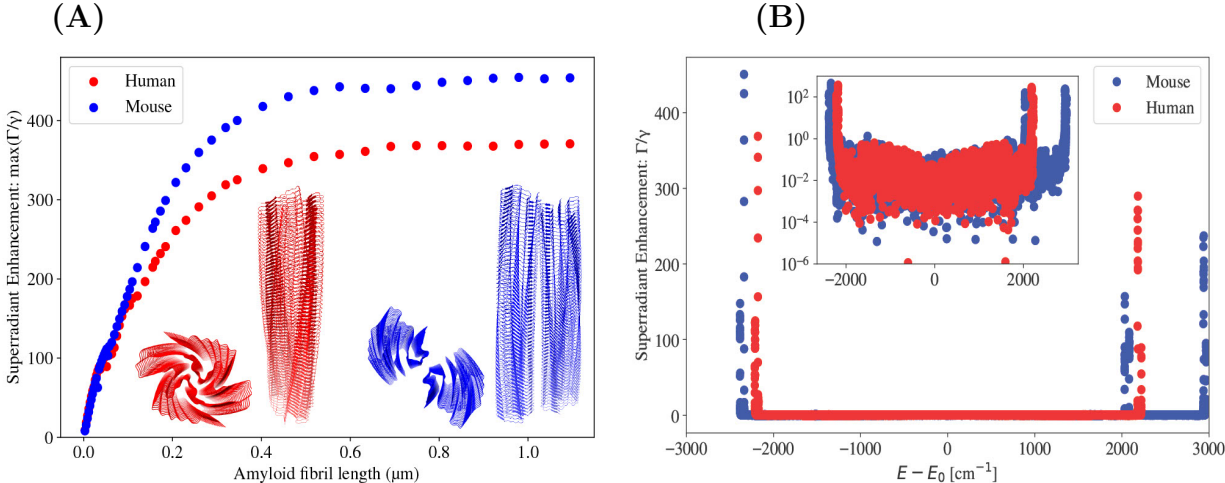


Figure 7: **(A)** Plot of the maximum superradiance $\max(\Gamma_j/\gamma)$ vs. structure length for model amyloid fibrils. Sample images of amyloid structures built from PDB files 6MST (*Homo sapiens*) and 6DSO (*Mus musculus*) are shown inset to the plot with their corresponding colors, both in a cross-sectional view and a longitudinal view. **(B)** The eigenvalue spectrum (Γ_j/γ vs $E - E_0$) of 864-nm 6MST (7200 tryptophan) and 6DSO (10800 tryptophan) amyloid fibrils. Inset is the same spectrum plotted with the y axis on a semi-log scale.

3.3 Amyloid fibrils

Fig. 7 presents the same data as in Fig. 5, but for single amyloid fibrils in human and in mouse. We will refer to the length of an amyloid fibril by its absolute length (in μm), and/or the number of subunits it is made of. The subunit of human (mouse) amyloid is given by the PDB entry 6MST (6DSO), contains 24 (36) Trp molecules, and is 2.88 nm in length. The Trp network of amyloid forms a helical pattern, which repeats approximately every 40 subunits (every 115.2 nm).

In panel 7(A), it can be seen that for both human and mouse amyloid fibrils, the maximum superradiant enhancement $\max(\Gamma/\gamma)$ reaches a saturating value at large lengths. For 1.09- μm human (mouse) amyloid fibrils, $\max(\Gamma/\gamma) = 371.21$ (453.14), far surpassing that of even a 2.2- μm 19-filament actin bundle, which has $\max(\Gamma/\gamma) = 160.93$. This is despite the Trp network in the amyloid fibrils being comprised of significantly fewer chromophores than that in actin. In fact, if one considers a human amyloid fibril and a 19-filament actin bundle that have the same number of Trp molecules (e.g., picking 1824 Trp molecules), the actin bundle has $\max(\Gamma/\gamma) = 37.70$, while the human amyloid fibril has $\max(\Gamma/\gamma) = 270$. This shows that the density of Trp chromophores within a unit volume and the transition dipole orientations of amyloid are much more suited for maintaining bright superradiant states than the Trp density and transition dipole orientations of actin bundles.

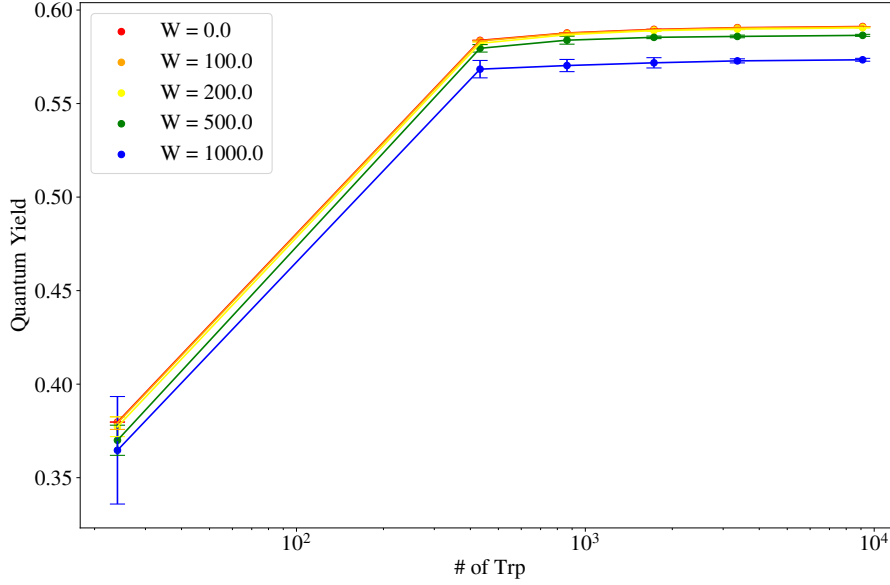


Figure 8: Thermal average of the quantum yield (QY) vs. number of tryptophan (Trp) molecules for varying static disorder strengths for human amyloid fibrils (pictured in Fig. 1(C)). W (in units of cm^{-1}) represents the strength of static disorder applied to (1), where each diagonal element of the effective Hamiltonian $H_{\text{eff},ii}$ is replaced by a random value in the range $[H_{\text{eff},ii} - W/2, H_{\text{eff},ii} + W/2]$. Then the Hamiltonian is diagonalized to find the eigenvalues, and from the eigenvalues the thermal average of the quantum yield is obtained. This is repeated ten times, and the mean is taken to obtain a data point. The error bars on each point represent one standard deviation of the ten QY values calculated for that point.

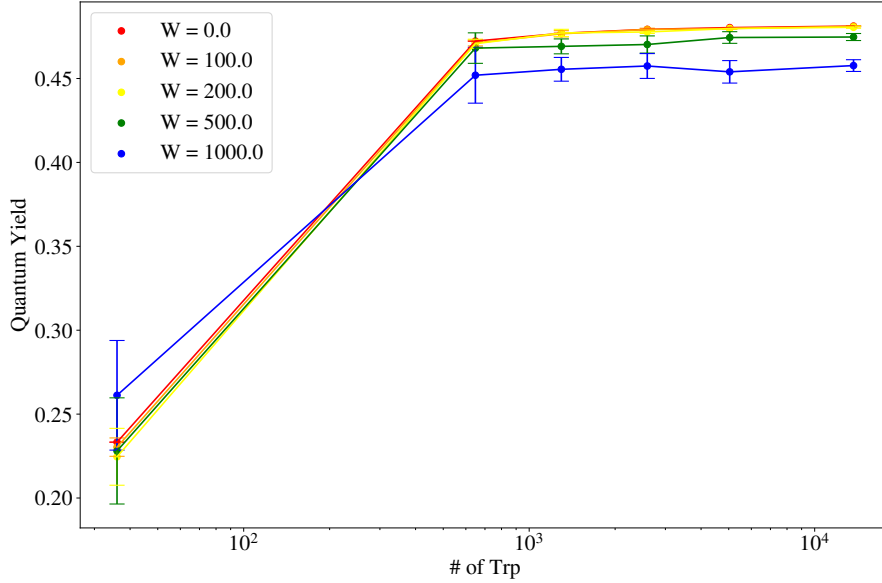


Figure 9: Thermal average of the quantum yield (QY) vs. number of tryptophan (Trp) molecules for varying static disorder strengths for murine amyloid fibrils (pictured in Fig. 1(D)). W (in units of cm^{-1}) represents the strength of static disorder applied to (1), where each diagonal element of the effective Hamiltonian $H_{\text{eff},ii}$ is replaced by a random value in the range $[H_{\text{eff},ii} - W/2, H_{\text{eff},ii} + W/2]$. Then the Hamiltonian is diagonalized to find the eigenvalues, and from the eigenvalues the thermal average of the quantum yield is obtained. This is repeated ten times, and the mean is taken to obtain a data point. The error bars on each point represent one standard deviation of the ten QY values calculated for that point.

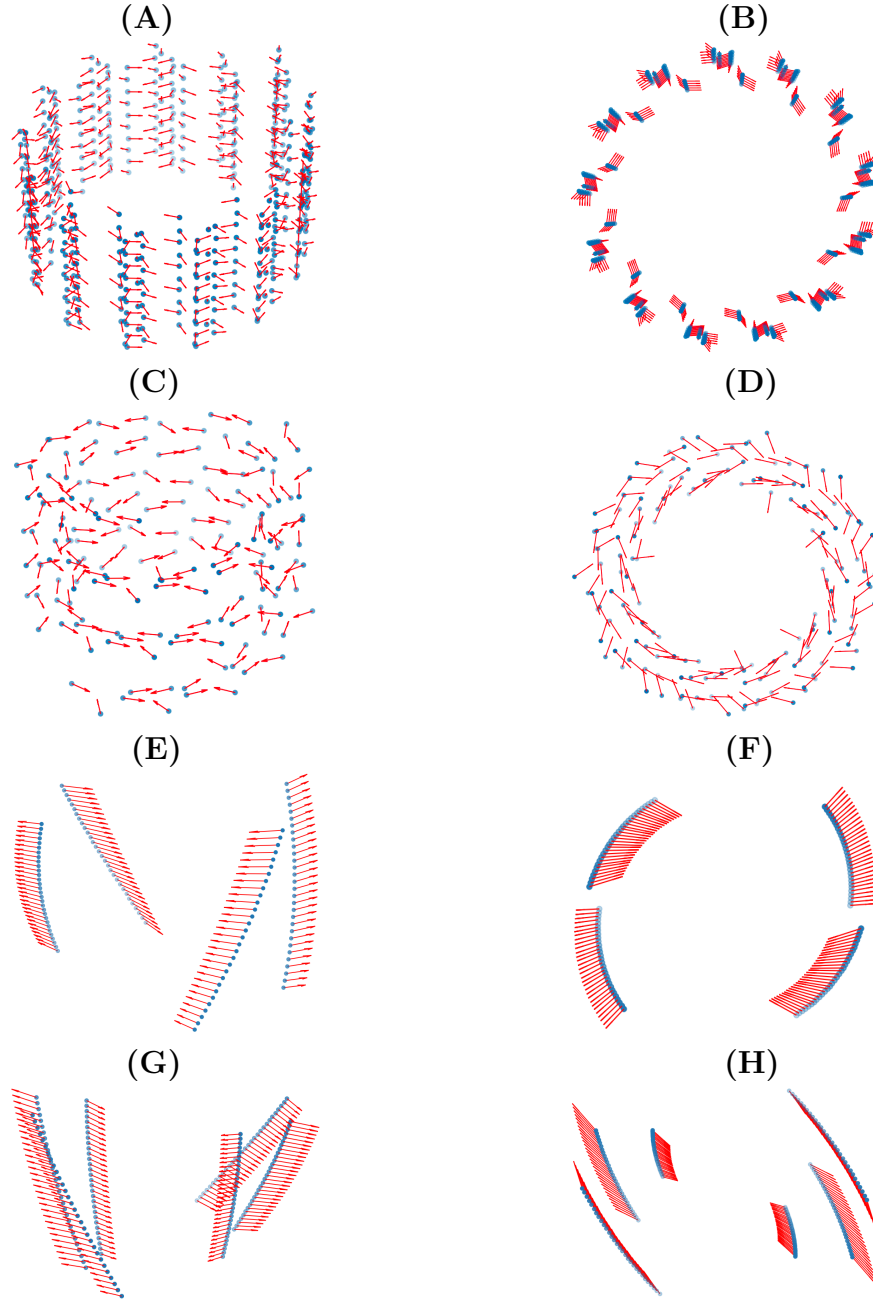


Figure 10: Transition dipole vector geometries of tryptophan (Trp) in the realistic biological structures considered in this paper. The blue dots represent the Trp molecules. Relative size of structures with respect to one another is not to scale. The size of vectors has been enlarged for viewing. **(A)** Angled longitudinal view of 45 nm microtubule (built from tubulin dimer PDB entry 1JFF). **(B)** Cross-sectional view of the microtubule. **(C)** Angled longitudinal view of 112.5 nm actin filament (built from actin subunit PDB entry 6BNO). **(D)** Cross-sectional view of the actin filament. **(E)** Angled longitudinal view of 20.16 nm human amyloid fibril (built from amyloid subunit PDB entry 6MST). **(F)** Cross-sectional view of human amyloid fibril. **(G)** Angled longitudinal view of 20.16 nm mouse amyloid fibril (built from amyloid subunit PDB entry 6DSO). **(H)** Cross-sectional view of mouse amyloid fibril.

In panel 7(B), we can see that superradiant states emerge at very specific bands in both the low- and high-energy portions of the spectrum, and at all other energies, the superradiant enhancement rate is very close to 0. For the human amyloid fibril (built from PDB file 6MST), the superradiant states are only present near the smallest and largest energies, and every other state is subradiant ($\Gamma_j < \gamma$, close to zero enhancement rate). The emergence of superradiant states only at a few energies arises due to the structure of the Trp networks in question, as discussed with the toy models in Section 2.3. Both amyloid fibril structures have dipole vector orientations that vary more smoothly from one dipole to its nearest neighbor, as compared with microtubules and actin filaments, which don't exhibit this feature (Fig. 10). The presence of a large proportion of superradiant states in the low-energy portion of the amyloid fibril spectrum gives it a very large QY, as seen in Figs. 8 and 9. Specifically, for system sizes of 864 Trp or above, the human (mouse) amyloid has a quantum yield between 0.55 and 0.60 (0.44 and 0.49) for all considered values of static disorder up to 1000 cm^{-1} ; these quantum yields are about two to three times that of actin filaments, and more than three to four times that of microtubules.

For the dependence of the amyloid fibril QY on static disorder, for 864nm structures, $\% \Delta \text{QY}(W : 0 \rightarrow 1000) = -3.05\%$ for human, and $\% \Delta \text{QY}(W : 0 \rightarrow 1000) = -5.01\%$ for mouse, making these fibrils at least as robust to static disorder as microtubules and actin filament bundles, and potentially more so. The QY of amyloid is also strongly enhanced with system size, with $\% \Delta \text{QY}(N : 1 \rightarrow 9120) = 130.65\%$ for human and $\% \Delta \text{QY}(N : 1 \rightarrow 13680) = 118.05\%$ for mouse, at zero static disorder. For $W = 1000 \text{ cm}^{-1}$, $\% \Delta \text{QY}(N : 1 \rightarrow 9120) = 128.88\%$ for human and $\% \Delta \text{QY}(N : 1 \rightarrow 13680) = 114.73\%$ for mouse. Thus, amyloid displays a very high QY that increases with system size, up to a certain point at which it begins to saturate: at zero static disorder, $\% \Delta \text{QY}(N : 432 \rightarrow 9120) = 1.26\%$ for human amyloid fibrils and $\% \Delta \text{QY}(N : 648 \rightarrow 13680) = 1.87\%$ for mouse amyloid fibrils, a clear indication of flattening of the monotonically increasing QY, as compared with the initial more-than-doubling and more-than-tripling of the QY from Trp alone in solution. For a human (mouse) amyloid fibril with greater than or equal to 432 (648) Trp molecules, the QY stays constant when $W = 1000 \text{ cm}^{-1}$ (any variation is within the error bars, i.e., random fluctuations caused by the static disorder).

It should be noted that for both amyloid fibrils, some inter-Trp distances are as small as $\sim 5 \text{ \AA}$. In the Hamiltonian (1), the point dipole approximation is made. But, in reality, the Trp molecule extends over space: the distance from the oxygen atom to the CZ2 atom in Trp is $\sim 7.7 \text{ \AA}$. The inter-Trp distances being smaller than the Trp molecules themselves means that orbitals of different Trp molecules may overlap, and this can lead to the formation of charge-transfer states, which are intermediate between an exciton and an electron donor-acceptor complex. Such charge-transfer states in biomolecular complexes with closely spaced chromophores have previously been described in DNA [47–49], proteins [50–52], and photosynthetic complexes [53]. In the case of our amyloid fibrils, strictly speaking, the point dipole approximation and the approximation of Trp as a two-level system would both break down. However, this only applies to the nearest-neighbor Trp-Trp interactions. For Trp molecules that are not as closely spaced (the majority of Trp-Trp pairs), the long-range terms that go as r^{-1} in Eqns. (8) and (9) are dominant over the r^{-2} and r^{-3} terms. Quantum coherent effects such as superradiance are greatly enhanced by this type of long-range interaction, and for these Trp molecules, the aforementioned approximations remain valid.

Due to the close Trp-Trp spacings in amyloid fibrils, we would expect the Trp-Trp couplings to be very high, and indeed they are. The average Trp-Trp coupling strength for a 100-subunit human (mouse) amyloid fibril, which has a length of 288 nm, is 0.971 cm^{-1} (0.741 cm^{-1}) with a standard deviation of 26.6 cm^{-1} (24.6 cm^{-1}). The nearest-neighbor Trp-Trp coupling for human (mouse) amyloid fibril is 1012 cm^{-1} (1306 cm^{-1}). As we expected, this leads to energies with much larger collective Lamb shifts for the lowest exciton states of amyloid fibrils, which can be seen in Fig. 7(B) at about -2500 cm^{-1} . This explains the very high quantum yield for amyloid fibrils (see Figs. 8 and 9): they have their brightest superradiant states at large negative shifts from the single-Trp excitation energy, thereby increasing the weight of these states in the thermal ensemble beyond those in either microtubules or actin bundles.

3.4 Energy gaps in the complex plane, and thermal robustness

We create plots of the energy gap ($\Delta\mathcal{E}$) in the complex plane for all the biological structures we study in this work. Let each complex eigenvalue of the non-Hermitian Hamiltonian (1) be denoted by \mathcal{E}_j , where the real and imaginary parts of \mathcal{E}_j are E_j and $-\frac{i}{2}\Gamma_j$, respectively. The energy gap in the complex plane is defined as

$$\Delta\mathcal{E} \equiv |\mathcal{E}_1 - \mathcal{E}_0|, \quad (3)$$

where $|\cdot|$ represents the complex norm, \mathcal{E}_0 is the state with the lowest energy and \mathcal{E}_1 is the state with the second lowest energy (i.e., $E_0 < E_j \ \forall j \neq 0$ and $E_1 < E_j \ \forall j \neq 0, 1$). This energy gap can be considered a measure of how “quantum mechanical” the system is and has been associated with robustness to thermal noise and supertransfer processes [2, 3, 39]. If the classical limit is taken for a quantum system (the limit $\hbar/S_{\text{sys}} \rightarrow 0$, where S_{sys} is the characteristic scale of the action of the system), then the spacing between the energy levels will approach 0. Therefore, as the system size increases, it would be conventionally expected that the system would become more classical, and thus exhibit a decrease in the energy gap.

In Fig. 11, $\Delta\mathcal{E}$ is plotted against structure length for single microtubules, 19-filament actin bundles, human amyloid fibrils, and mouse amyloid fibrils. In microtubules, we can observe an *increase* in the energy gap from around 100 nm to 280 nm. Since 280 nm is the excitation wavelength of Trp, this means that the system increases its energy gap up to this characteristic length scale induced by matter interacting with the electromagnetic field. This observation has been made in [2]. Interestingly, we do not see this behavior for any of the other structures in Fig. 11. For both amyloids (panels (C) and (D) in Fig. 11), there is a huge peak of the energy gap around 10-25 nm, and then a smooth dropoff that tends to 0. The maximum energy gap of human (mouse) amyloid is 40.32 cm^{-1} (60.47 cm^{-1}), which is about 47 (71) times larger than the maximum energy gap of microtubules around 280 nm, which is 0.85 cm^{-1} . Even though the energy gap of amyloid is decreasing at the excitation wavelength of Trp (280 nm), its value for human (mouse) amyloid fibrils at this length is 0.278 cm^{-1} (0.344 cm^{-1}), which is on the same order as the energy gap of microtubules. This is consistent with the robustness of amyloid fibrils compared with microtubules.

The energy gap behavior of 19-filament actin bundles (panel (B) from Fig. 11) is vastly different from all the other structures. It has a sporadic behavior that does not trend upward

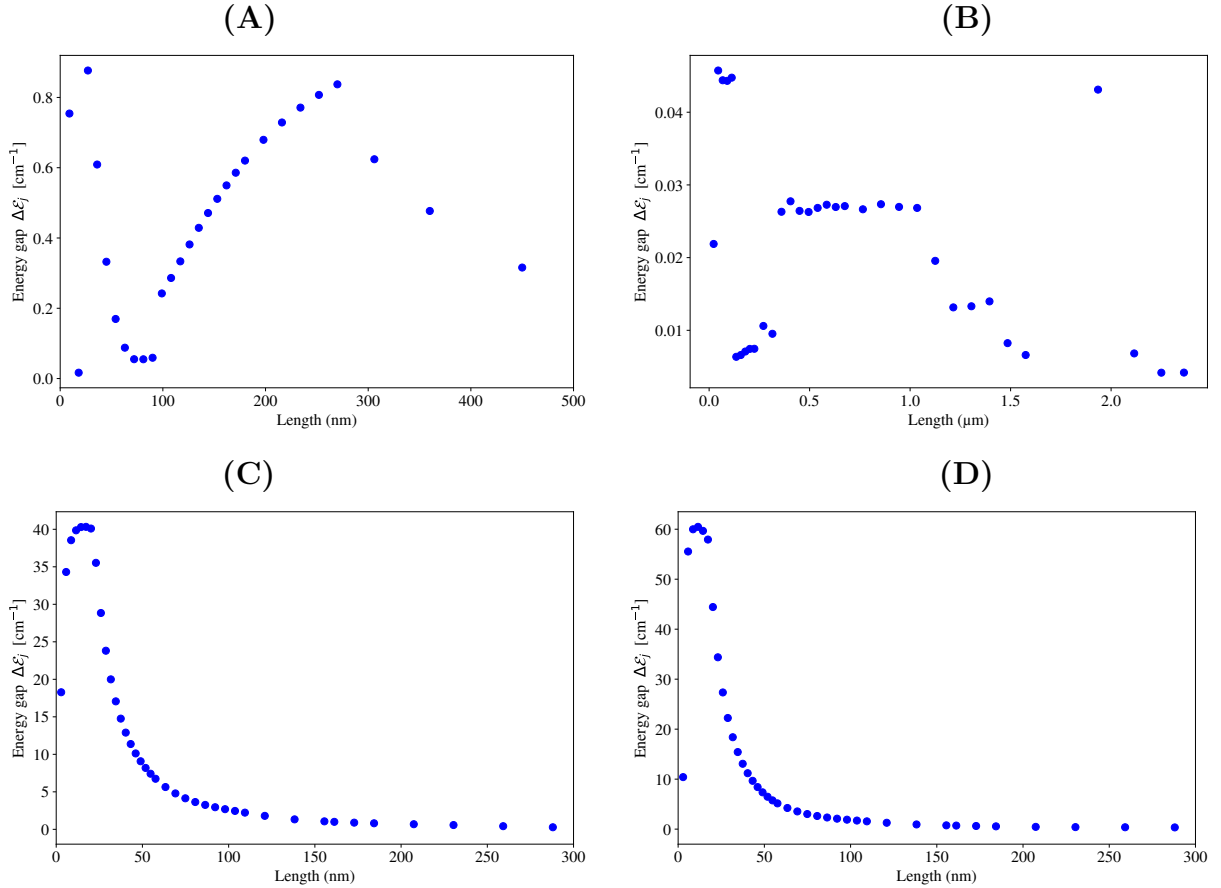


Figure 11: Plots of the energy gap $\Delta\mathcal{E}$ in the complex plane, given by Eq. (3), vs. length. The energy gap is calculated using the eigenspectrum obtained by diagonalizing the non-Hermitian Hamiltonian (1) for the tryptophan networks in biological structures. **(A)** Energy gap plot for single microtubules (pictured in Fig. 1**(A)**). **(B)** Energy gap plot for 19-filament actin bundles. A top-down view of a 19-filament actin bundle is pictured inset in Fig. 5**(A)**, and a single filament is pictured in Fig. 1**(B)**. **(C)** Energy gap plot for human amyloid fibrils (pictured in Fig. 1**(C)**). **(D)** Energy gap plot for murine amyloid fibrils (pictured in Fig. 1**(D)**).

with increasing system size. The maximum energy gap for 19-filament actin bundles is at $\sim 0.045 \mu\text{m}$, and it is 0.046 cm^{-1} , which is a whole order of magnitude below the maximum energy gap of microtubules, and three orders of magnitude less than the maximum energy gap of amyloid. The sporadic behavior and low values for the energy gap for actin may reflect the more strictly mechanical nature of actin bundles compared with the other structures studied in this work. However, a more comprehensive analysis of these energy gaps averaged over multiple realizations of different static disorder strengths is warranted, to understand better how the transition to classicality in these structures is affected by a thermal environment.

4 Discussion

We discuss here the implications of our findings of high quantum yield and robustness for microtubules, actin bundles, and amyloid fibrils. In Alzheimer’s disease and related dementias, the prevailing theory is that amyloid plaque formation is a direct cause of the onset of the disease [38]. Based on our results we propose an alternative hypothesis to these previous observations on amyloid. By definition, if the QY of a structure was 1, then every photon that it absorbed would be re-emitted into the environment. We have predicted here that the QY of even small human amyloid fibrils $< 1\mu\text{m}$ is over 0.5. Given the significant absorption-emission Stokes shift of Trp, every photon that is re-emitted will be redshifted to a much lower energy than the UV photon that was absorbed, indicating that amyloid may serve a photoprotective role that downconverts dangerous UV photons in the brain to lower-energy photons which can be safely managed. Lower QY structures like microtubules and actin may assist with this process as well.

Table 1 shows the decay rate values of the most superradiant and most subradiant states, along with other key observables associated with these diverse neuroprotein architectures. One trend we can see in Table 1—and according to which it is organized—is that the maximum superradiance of the axon bundles is the highest ($\tau_{\text{super}} \propto 1/\max(\Gamma_j)$), and as we go down the table, this value decreases for the other protein structures, with the smallest maximum superradiance (longest superradiant lifetime) belonging to the single actin filament. Large bundles of long, stably configured, straight microtubules in axons can exhibit enhanced, robust superradiance several thousands of times the single-Trp decay rate [3], suggesting possible routes for quantum information processing in the brain that would be at least nine orders of magnitude faster than Hodgkin-Huxley chemical signaling at the millisecond scale in spiking neurons.

After the microtubule-based structures, amyloid fibrils in both humans and mice have the next largest superradiant power outputs ($E_{\text{super}}/\tau_{\text{super}}$), both due to their high-energy clustering of superradiant states and their picosecond-scale superradiant lifetimes. Interestingly, among the protein structures we consider in Table 1, the maximum superradiant density ($\max(\Gamma_j)/N\gamma$) is the highest for a single microtubule of 320 nm (0.120) and a human amyloid fibril of 346 nm (0.113). Protein aggregates supporting such superradiant states with high power outputs could dissipate high-energy UV photons in an intensely oxidative cellular environment more quickly, and mitigate any potential damage. This is especially important in neuropathological conditions such as Alzheimer’s, but also in a host of other complex diseases characterized by high allostatic load and oxidative stress, where high-energy photons

Protein Structure, Length in nm	$\frac{\max(\Gamma_j)}{N\gamma}$	τ_{super} (ps)	$\mathcal{P}_{\text{super}}$ (μW)	$\frac{\min(\Gamma_j)}{\gamma}$	τ_{sub} (s)
91-MT Axon, 320 (fit)	0.012	0.428	1.65	—	—
61-MT Axon, 320 (fit)	0.016	0.479	1.47	—	—
Centriole, 400	0.028	0.495	1.42	4.6×10^{-8}	0.042
61-MT Axon, 224	0.020	0.547	1.30	3.6×10^{-10}	5.4
37-MT Axon, 320	0.026	0.602	1.19	2.3×10^{-10}	8.5
91-MT Axon, 152	0.017	0.636	1.13	2.6×10^{-10}	7.5
Axoneme (1JFF), 320	0.031	0.754	0.93	2.8×10^{-10}	6.9
19-MT Axon, 320	0.032	0.769	0.92	9.9×10^{-10}	2.0
7-MT Axon, 640	0.039	0.856	0.81	1.4×10^{-10}	13.9
7-MT Axon, 320	0.071	0.941	0.75	2.8×10^{-9}	0.69
Axoneme (6U42), 320	0.010	2.64	0.26	1.0×10^{-8}	0.19
1 Microtubule, 320	0.120	3.89	0.18	1.36×10^{-6}	0.001
Murine amyloid, 1094	0.033	4.29	0.15	8.2×10^{-8}	0.024
Murine amyloid, 346	0.093	4.85	0.14	3.27×10^{-7}	0.006
Human amyloid, 1094	0.041	5.24	0.13	6.41×10^{-8}	0.030
Human amyloid, 346	0.113	5.98	0.11	1.47×10^{-7}	0.013
19-F actin bundle, 2250	0.003	12.1	0.059	5.00×10^{-6}	3.89×10^{-4}
19-F actin bundle, 450	0.012	13.1	0.054	5.01×10^{-6}	3.88×10^{-4}
7-F actin bundle, 2700	0.002	46.0	0.015	5.18×10^{-6}	3.75×10^{-4}
7-F actin bundle, 450	0.007	61.0	0.012	5.18×10^{-6}	3.75×10^{-4}
1-F actin, 2700	0.003	197	0.004	0.006	3.16×10^{-7}
1-F actin, 450	0.014	222	0.003	0.007	2.81×10^{-7}

Table 1: Values for the extremal superradiant and subradiant decay rate values calculated by diagonalizing the non-Hermitian Hamiltonian in Eq. (1) for the tryptophan (Trp) network in each protein structure. “MT” stands for microtubule; the “-F” stands for “filament.” Images of a microtubule, 1-F actin, human amyloid, and murine amyloid, are shown in Fig. 1(A)-(D), respectively. For the first eleven rows with structures not analyzed in this paper, the values were taken from [3]. For the last two columns of the first two rows, the “—” indicate that an analytical fit was taken of the equivalent of Figs. 5 and 7 for those structures. So, subradiant data was not available for these structures: only superradiance data was available. See [3] for more details. The column $\max(\Gamma_j)/N\gamma$ represents the value of the maximum decay rate from the eigenspectrum (the enhancement rate of the maximally superradiant state). It is normalized by the single-Trp decay rate $\gamma \approx 2.73 \times 10^{-3} \text{ cm}^{-1}$ and the number of emitters N , which varies for each structure. The column $\tau_{\text{super}} = (2\pi c \max(\Gamma_j))^{-1}$ is the lifetime of the maximally superradiant state in picoseconds. The column $\mathcal{P}_{\text{super}}$ represents the power output $E_{\text{super}}/\tau_{\text{super}}$ of the superradiant state. In the next portion of the table, information about the long-lasting subradiant states is listed. The column $\min(\Gamma_j)/\gamma$ is the maximally subradiant state (the one with the smallest Γ_j). The column $\tau_{\text{sub}} = (2\pi c \min(\Gamma_j))^{-1}$ is the lifetime of the maximally subradiant state in seconds.

can be produced due to metabolic photon emissions. Our prediction of high power outputs for amyloid fibrils supports the hypothesis that amyloid fibrils and plaques could actually serve as photoprotective entities in the brain.

We also see in Table 1 the general trend of highly subradiant long-lived states correlated with highly superradiant short-lived states. (τ_{sub} generally decreases down the table, while τ_{super} strictly increases down the table.) Subradiant states have been predicted with high excitonic occupation probabilities on the inner lumen surface of microtubules, while superradiant states have more delocalized occupation probabilities but with a preference for the external microtubule surface (see Fig. 4 of [2]). The lifetime of such superradiant states is faster than thermal noise from the aqueous environment surrounding the microtubule, whereas the lumen surface of the microtubule is exposed to a more ordered, gel-like matrix, and is thus subjected to far less thermal fluctuation. Such a locally protected environment could enable the potential exploitation of subradiant states (which are not particularly robust to noise) by living systems, possibly serving as a collective quantum mechanism for synchronizing behavior and information processing over long periods. (τ_{sub} values in Table 1 are on the order of microseconds to tens of seconds.) In quantum information applications, the long lifetime of subradiant states in qubit architectures has been used to create very long-lived quantum memories [54], implement mechanisms for lossless transport of photons [55], and generate phase-imprinting for potential quantum storage of multiphotonic qubits in two-level systems [56].

Also, the quantum yield of amyloid may be even larger than we have predicted here. In the β -sheets displayed in Fig. 2(B), we can see that there are so-called short hydrogen bonds (SHBs) that connect the β -strands side-by-side (labeled by dashed black lines). Even in the absence of aromatic chromophores like Trp, networks of these SHBs have been observed to absorb strongly in the UV band through proton transfer events, and emit in the visible band [57, 58]. This means that, like Trp, networks of SHBs may aid in downconverting UV photons to lower energies. Networks of SHBs in amyloid fibrils may therefore exhibit their own bright superradiant states and enhance the QY of amyloid even beyond what we predict in this work. Due to the incredibly high QY of amyloid fibrils and its potential for photoprotection, rather than being a cause of pathological conditions, amyloid fibrils could be a *response* to them, and to the highly oxidative environments that characterize them. Therapies that target amyloid in the brain for elimination could therefore exacerbate such diseases rather than ameliorating them.

There are at least 37 known proteins that form pathological amyloids [34]. We have found that the amyloids 6MST and 6DSO, which are associated with systemic AA amyloidosis [59], exhibit extremely robust QY. Since amyloids are a geometric class of protein architectures characterized by helical superstructures made of β -sheets, it is likely that amyloids formed from other proteins (such as lysozyme, insulin, and IAPP) will have similar transition dipole networks as discussed in Section 2.3, and thus may also exhibit the high QYs that would play a strongly photoprotective role in the pathological cellular environment.

Furthermore, the formation of structures called cofilin-actin rods from pools of actin and the cofilin protein have also been studied [60–62], with recent suggestions of potentially quantum behavior being disrupted in Alzheimer’s pathogenesis [62]. Cofilin-actin rods do have a helical structure: every subunit that is added to the rod comes with an approximate 5° twist [61]. Therefore, without having conducted any of the detailed analyses presented here

for microtubules, actin bundles, and amyloid fibrils, we would hypothesize that cofilin-actin rods exhibit significant superradiance that may translate into robust, observable quantum yield effects based on the symmetry and interactions of their helical Trp networks. This is yet another instance in which a cylindrically or helically symmetric structure is created in the context of neurodegeneration, further stressing the importance of chromophore network geometry in protein lattices as the source of these robust superradiant effects.

As the microtubule results in the Supplementary Material and in Section 3.1 attest, the morphology and mechanical deformations of protein structures are crucial to understanding the modulation of superradiant effects. For example, amyloid fibrils are known to aggregate into macroscopic structures called amyloid plaques, together with glial and neuritic debris [63]. They are found in the grey matter of the brain in the areas associated with memory and cognition. Amyloid plaques can form spherically symmetric aggregates of amyloid fibrils with very dense cores [64]. Plaques have also been observed to form symmetric superarchitectures such as bundles, as well as mesh-like and star-like geometries [65]. Given these observations, amyloid plaques may exhibit even higher, more robust superradiance and quantum yield values than those of single fibrils, which would strengthen the argument of amyloid’s photoprotective role and of the mitigating effect of plaque formation in neurodegenerative pathology.

Our predictions of robust, observable increases in the QY for Trp networks in large protein polymeric architectures has implications for many other diseases outside the neurodegenerative context. For example, sickle-cell anemia results from a Glu \rightarrow Val mutation of the amino acid at the sixth position on the beta chain of normal hemoglobin (HbA). The resulting deoxygenated hemoglobin (HbS) is known to aggregate in erythrocytes (red blood cells without nuclei) [66, 67] and form helical structures. These helical hemoglobin strands, commonly known as Wishner-Love helices, would then manifest helical Trp networks. We have found that helical Trp networks exhibit superradiance in three distinct cases (in microtubules, actin filaments, and amyloid fibrils), so hemoglobin’s helical Trp network may also exhibit significant superradiance and/or quantum yield. If these hemoglobin aggregates are indeed found to exhibit superradiance and robust increases in QY with increasing size, then quantum-enhanced photoprotection may also play an important role in the onset, progression, and treatment of hemoglobinopathies like sickle-cell, which are also associated with intensely oxidative and damaging cellular environments.

Our results pose opportunities for a paradigm shift in the theory of neuronal information processing and signaling. The role of microtubules in information processing in the brain has been studied extensively [23, 68–70]. Also, classical energy scalings cannot account for the sub-neuronal information processing capacity of the brain [71], given its extremely low input power of around 20 W. There must be another physical mechanism that enables the human brain to achieve the computational efficiency that it does, at orders of magnitude lower power consumptions than high-performance hardware systems. A tantalizing possibility is that extended protein architectures, such as those described here and elsewhere [2, 3], including axons in the brain, may form a highly interconnected, ultrafast quantum-optical network that gives rise to incredibly efficient transfer and processing of information. This mechanism would be much faster than chemical Hodgkin-Huxley-type transport based on neuronal sodium-potassium gradients firing at the millisecond timescale, which is currently used as a standard paradigm in neuroscience.

5 Conclusion and Future Plans

We analyze the interaction of the electromagnetic field with networks of tryptophan chromophores. Geometrical information on these networks and the orientations of the tryptophan transition dipoles are extracted from realistic simulations of three types of neuroprotein architectural elements: microtubules, actin filaments/bundles, and amyloid fibrils. The tryptophan chromophores are modeled as two-level systems and exhibit superradiant behavior as a collective when coherently superposed in the single-excitation limit. We see this by diagonalizing the non-Hermitian Hamiltonian used to describe the collective light-matter interaction of such a weakly photoexcited system. All three structures were found to exhibit bright superradiant states due to symmetry and long-range couplings, which support robustness of the quantum yield as a figure of merit with increasing static disorder even up to five times room-temperature energy. In the case of microtubules and amyloid fibrils, the brightest superradiant states are clustered near the lowest-energy portion of their spectra, and these photophysical properties result in a large quantum yield that counterintuitively increases with system size and has been experimentally confirmed for microtubules [3].

Our results display the observable and important consequences that quantum coherent effects have on neuroprotein architectures. These analyses could strengthen our understanding of the etiology of neurodegenerative and other complex diseases, which are frequently characterized by anomalous protein polymers. Furthermore, our investigations of superradiance and subradiance in these neuroproteins are revealing an ultrafast mechanism that our brains may use to process information, which is paired with an extremely long-lived mechanism for coordinating biological function. This work contributes significantly to our understanding of how quantum biology can speed up, enhance, and optimize behavior in the “wetware” environments of living systems. Acknowledging the wide body of research that has been conducted on ultraweak and metabolic photon emissions in the cell, we have incorporated the interaction of neuroprotein tryptophan lattices with the electromagnetic field via the equations of quantum optics, giving us a totally different lens with which to view biology. Such a paradigm shift can greatly enhance our understanding of nature, to visualize biological architectures as chromophore lattices synchronized by long-range interactions, and imbued with unique and specific photophysical properties that are enhanced by collective light-matter interactions governed by the equations of quantum optics. Such a shift reflects a return to understanding, in the (paraphrased) words of Richard Feynman and with the ancients, how external light from the fiery sun causes trees and plants to grow from the carboniferous air; and in parallel symbiosis how oxygen-metabolizing organisms may have evolved their protein architectures to exploit “internal” photonic emissions for information processing and to mitigate potentially damaging wavelengths in the cell.

Future work will include performing experiments in order to verify the quantum yield predictions that we have made here. Analogous to prior work [3], where the increased quantum yield in microtubules from tubulin dimers in solution was unambiguously associated with the increased radiative rate due to superradiance, we now have a clear path and approach to experimental validation of collective quantum optical behavior in a wide class of protein polymeric aggregates in solution. We hope that this work will stimulate further experimental efforts in this regard.

6 Methods

6.1 Physical model

In this work we model tryptophan (Trp), a strongly fluorescent amino acid in the ultraviolet (UV) band, as a two-level system [5] with transition energy $e_0 \approx 280 \text{ nm} = 3.57 \times 10^4 \text{ cm}^{-1}$ and decay rate $\gamma \approx 2.73 \times 10^{-3} \text{ cm}^{-1}$ [4,69]. Trp has a large transition dipole moment of ~ 6.0 debye. We use a non-Hermitian Hamiltonian to describe the interaction of a N -dimensional Trp network with the electromagnetic field [72–76]

$$H_{\text{eff}} = H_0 + \Delta - \frac{i}{2}G \quad (4)$$

where

$$H_0 = \sum_{n=0}^{N-1} \hbar\omega_0 |n\rangle\langle n| \quad (5)$$

$$\Delta = \sum_{n \neq m}^N \Delta_{nm} |n\rangle\langle m| \quad (6)$$

$$G = \sum_{n=0}^{N-1} \gamma |n\rangle\langle n| + \sum_{n \neq m}^N G_{nm} |n\rangle\langle m| \quad (7)$$

$$\begin{aligned} \Delta_{nm} = \frac{3\gamma}{4} \left[\left(-\frac{\cos(\alpha_{nm})}{\alpha_{nm}} + \frac{\sin(\alpha_{nm})}{\alpha_{nm}^2} + \frac{\cos(\alpha_{nm})}{\alpha_{nm}^3} \right) \hat{\mu}_n \cdot \hat{\mu}_m \right. \\ \left. - \left(-\frac{\cos(\alpha_{nm})}{\alpha_{nm}} + 3\frac{\sin(\alpha_{nm})}{\alpha_{nm}^2} + 3\frac{\cos(\alpha_{nm})}{\alpha_{nm}^3} \right) (\hat{\mu}_n \cdot \hat{r}_{nm})(\hat{\mu}_m \cdot \hat{r}_{nm}) \right] \quad (8) \end{aligned}$$

$$\begin{aligned} G_{nm} = \frac{3\gamma}{2} \left[\left(\frac{\sin(\alpha_{nm})}{\alpha_{nm}} + \frac{\cos(\alpha_{nm})}{\alpha_{nm}^2} - \frac{\sin(\alpha_{nm})}{\alpha_{nm}^3} \right) \hat{\mu}_n \cdot \hat{\mu}_m \right. \\ \left. - \left(\frac{\sin(\alpha_{nm})}{\alpha_{nm}} + 3\frac{\cos(\alpha_{nm})}{\alpha_{nm}^2} - 3\frac{\sin(\alpha_{nm})}{\alpha_{nm}^3} \right) (\hat{\mu}_n \cdot \hat{r}_{nm})(\hat{\mu}_m \cdot \hat{r}_{nm}) \right] \quad (9) \end{aligned}$$

where $\alpha_{nm} \equiv k_0 r_{nm}$. The constants k_0 and ω_0 are defined in terms of e_0 by $k_0 = 2\pi e_0 \times 10^{-8}$ and $\omega_0 = 2\pi e_0 c / n_r \times 10^{-8}$ where $n_r \approx \sqrt{\varepsilon_r}$ is the refractive index assuming that relative permeability is 1. The vector \hat{r}_{nm} is the unit vector pointing from the n^{th} site to the m^{th} site in physical space, and r_{nm} is the distance between the n^{th} and m^{th} sites. The unit vector $\hat{\mu}_n$ is the transition dipole moment of the n^{th} site.

6.2 Quantum Yield

The quantum yield (QY) is a dimensionless number from 0 to 1 that is defined to be the ratio of the number of photons emitted to the number of photons absorbed. Equivalently, it

can be written as

$$\text{QY} \equiv \frac{\Gamma}{\Gamma + \Gamma_{nr}} \quad (10)$$

where Γ is the collective radiative decay rate, and Γ_{nr} is the non-radiative decay rate. It ranges from 0 to 1. If the QY is close to 1, that means that most photons that get absorbed get re-emitted, and if the QY is close to 0, that means that most photons that get absorbed don't get re-emitted. Trp is known to have a significant absorption-emission Stokes shift [3], so photons will be re-emitted at a lower energy than that of their absorption. Therefore, if a Trp network has a high QY, it can be inferred that the Trp network will act in a photoprotective role against high-energy UV photons: absorbing them and then “downconverting” (red-shifting) them to a lower energy.

Since biological structures exist in a warm and wet environment, we take the thermal average of our quantities. Firstly, the partition function Z is given by

$$Z = \sum_{j=0}^{N-1} \exp(-\beta E_j) \quad (11)$$

where $\beta \equiv (k_B T)^{-1}$. The thermal average of the decay rate is then

$$\langle \Gamma \rangle_{th} = \frac{1}{Z} \sum_{j=0}^{N-1} \Gamma_j \exp(-\beta E_j). \quad (12)$$

This allows us to calculate the thermal average of the QY

$$\langle \text{QY} \rangle_{th} = \frac{\langle \Gamma \rangle_{th}}{\langle \Gamma \rangle_{th} + \langle \Gamma_{nr} \rangle_{th}}. \quad (13)$$

We take $\langle \Gamma_{nr} \rangle_{th} = \gamma_{nr}$ in this case, assuming conservatively that there is no reduction in the non-radiative decay rate leading to an increase in the QY. This represents the assumption that Trp network formation in protein introduces no change in the non-radiative decay channels, as compared with Trp alone in solution. Recent experimental evidence [3] indicates that Trp network formation in tubulin actually *increases* the non-radiative decay rate, suggesting that the protein environment competes with superradiant enhancements to modulate the observed QY.

6.3 Biological structures

We model three sets of biological structures in this paper: microtubules, actin filaments, and amyloid fibrils. Python scripts that implement all the following procedures and generate all PDB files for structures of a given length can be found in a GitHub repository link in the Data Availability Statement, which will be made available after publication.

6.3.1 Microtubules

We construct models of microtubules of varying length from the tubulin dimer stored in the Protein Data Bank (PDB) entry 1JFF [77] as per the methods given in Appendix A of [2] and Section S3 in [3]. We briefly summarize the procedure here.

Many identical 1JFF tubulin dimers are laid next to one another to form a left-handed helical microtubule structure with a diameter of 22.4 nm. The initial orientation of one tubulin dimer is such that the α and β chains lie both along the protofilament direction. Let this be the x-axis. Then, each tubulin dimer is acted on by the following initial operations: (1) rotated by -55.38° about its longitudinal axis, (2) rotated by 11.7° about the β -tubulin Trp346 CD2 atom, and (3) translated by 11.2 nm in the y-direction and 0.3 nm in the z-direction. After applying operations (1)-(3) to each tubulin dimer, a set of operations is applied N times to the N th dimer to form a single spiral (one spiral consists of 13 tubulin dimers, so $N \leq 13$): (4) rotation of 27.69° about the x-axis and (5) translation of 0.9 nm in the x-direction. This generates a 13-dimer spiral. To create microtubules with multiple spirals, each spiral is translated multiples of 80 nm in the x-direction from the initial spiral. This procedure creates microtubules with a radius of ~ 11.2 nm (from the microtubule longitudinal axis to the tubulin dimer center-of-mass), approximately intermediate between the outer (cytoplasm-surface) radius of ~ 13.5 nm and the inner (lumen-surface) radius of ~ 9.5 nm.

After creating a microtubule, the positions and transition dipole moments of the 8 atoms in every Trp molecule are extracted. The position of a Trp molecule is given by the midpoint of the positions of the CD2 and CE2 carbon atoms in it. The transition dipole moment of a Trp molecule is taken as the well-known 1L_a transition of Trp [5, 78], which is the vector pointing 46.2° above the axis joining the midpoint between the CD2 and CE2 carbons and carbon CD1, in the plane of the indole ring (i.e. towards nitrogen NE1).

6.3.2 Actin filaments and actin filament bundles

We construct models of actin filaments of varying length from the PDB entry 6BNO as per the description of the structure given in [79]. The procedure to generate actin filaments of a specified length is summarized below.

Many identical 6BNO bare actin filaments are laid next to one another to form a right-handed helical filament. Let the longitudinal direction of the filament be defined as the x-axis. Then, the following operations are applied N times to the N th filament: (1) translation of 22.488 nm in the x-direction and (2) rotation by -253.2° about its own axis (the x-axis). This creates actin filaments consisting of any number of 6BNO bare filaments. Extraction of Trp positions and transition dipole moments are the same as for microtubules.

We also take many actin filaments constructed in this way, and pack them together in concentric hexagons, forming actin bundles. This creates bundles containing $3N^2 - 3N + 1$ filaments, where N is the number of concentric hexagons, including the center. We create and study 7-filament ($N = 2$) and 19-filament ($N = 3$) bundles.

6.3.3 Amyloid fibrils

We construct models of human (mouse) amyloid fibrils of varying length from the PDB entries 6MST (6DSO), respectively, as per the descriptions of the structures given in [59]. The procedure to generate amyloid fibrils of a specified length is summarized below. For both human and mouse amyloid, each subunit is characterized by a six-strand β -sheet structure, where each β strand is joined to its neighbor via hydrogen bonds. The entire fibril is also

known as a β helix.

Many identical 6MST (6DSO) amyloid fibrils are laid next to one another to form a right(left)-handed helical fibril. Before applying the necessary operations, we find that a preliminary translation is required for each 6MST (6DSO) fibril: -14.0474 (-14.1715) nm in the x-direction, -14.0376 (-14.1595) nm in the y-direction, and -14.0039 (-11.8823) nm in the z-direction. This moves the center of mass of the molecule to the origin, so that subsequent rotations are performed along the axis parallel to the would-be fibril direction that passes through the center of mass. Let this axis be defined as the x-axis. Then, the following operations are applied N times to the N th fibril for 6MST: (1) translation of 2.88 nm in the x-direction and (2) rotation by 9.24° about its own axis (the x-axis). For 6DSO, the translation is the same², but the rotation is -6.90° about its own axis. This creates actin filaments consisting of any number of amyloid fibrils. Extraction of Trp positions and dipole moments are the same as for microtubules.

Conflict of Interest Statement

The authors declare that the research was conducted in the absence of any commercial or financial relationships that could be construed as a potential conflict of interest.

Author Contributions

HP: Data curation, Formal analysis, Investigation, Software, Validation, Visualization, Writing – original draft, Writing – review & editing; NSB: Data curation, Investigation, Software, Validation, Visualization; PK: Conceptualization, Funding acquisition, Methodology, Project administration, Resources, Supervision, Visualization, Writing – original draft, Writing – review & editing.

Funding

This work was supported in parts by the Alfred P. Sloan Foundation, Guy Foundation (UK), and Chaikin-Wile Foundation.

Acknowledgments

This research used resources of the Argonne Leadership Computing Facility, a U.S. Department of Energy (DOE) Office of Science user facility at Argonne National Laboratory and is based on research supported by the U.S. DOE Office of Science-Advanced Scientific Computing Research Program, under Contract No. DE-AC02-06CH11357. Portions of the manuscript were drafted and discussed during PK’s 2023 residency as a Fellow of the

²In [59], the translations for 6DSO and 6MST are different. We chose to make this modification after our own analysis of the structure.

Kavli Institute for Theoretical Physics (KITP), which was supported in part by grant NSF PHY-1748958 to KITP.

Supplemental Information

In the Supplemental Information, we present plots of the eigenvectors obtained by diagonalizing the non-Hermitian Hamiltonian (1) for the Trp network of mechanically deformed single microtubules. Each eigenvector is projected onto the site basis, and the color on each Trp represents the probability that it is excited. We would like to thank Marco Agostino Derru for providing us the atomistic structures of these deformed microtubules for the various vibrational and torsional modes presented.

References

- [1] R. H. Dicke. Coherence in spontaneous radiation processes. *Phys. Rev.*, 93:99–110, Jan 1954.
- [2] G L Celardo, M Angeli, T J A Craddock, and P Kurian. On the existence of superradiant excitonic states in microtubules. *New Journal of Physics*, 21(2):023005, feb 2019.
- [3] N. S. Babcock, G. Montes-Cabrera, K. E. Oberhofer, M. Chergui, G. L. Celardo, and P. Kurian. Ultraviolet superradiance from mega-networks of tryptophan in biological architectures. *The Journal of Physical Chemistry B*, 128(17):4035–4046, April 2024.
- [4] Philip Kurian, TO Obisesan, and Travis JA Craddock. Oxidative species-induced excitonic transport in tubulin aromatic networks: Potential implications for neurodegenerative disease. *Journal of Photochemistry and Photobiology B: Biology*, 175:109–124, 2017.
- [5] Patrik R. Callis. [7] 1La and 1Lb transitions of tryptophan: Applications of theory and experimental observations to fluorescence of proteins. In *Flourescence Spectroscopy*, volume 278 of *Methods in Enzymology*, pages 113–150. Academic Press, 1997.
- [6] Gregory S Engel, Tessa R Calhoun, Elizabeth L Read, Tae-Kyu Ahn, Tomáš Mančal, Yuan-Chung Cheng, Robert E Blankenship, and Graham R Fleming. Evidence for wavelike energy transfer through quantum coherence in photosynthetic systems. *Nature*, 446(7137):782–786, 2007.
- [7] Gitt Panitchayangkoon, Dugan Hayes, Kelly A Fransted, Justin R Caram, Elad Harel, Jianzhong Wen, Robert E Blankenship, and Gregory S Engel. Long-lived quantum coherence in photosynthetic complexes at physiological temperature. *Proceedings of the National Academy of Sciences*, 107(29):12766–12770, 2010.
- [8] Elisabetta Collini, Cathy Y Wong, Krystyna E Wilk, Paul MG Curmi, Paul Brumer, and Gregory D Scholes. Coherently wired light-harvesting in photosynthetic marine algae at ambient temperature. *Nature*, 463(7281):644–647, 2010.

- [9] Johan Strümpfer, Melih Sener, and Klaus Schulten. How quantum coherence assists photosynthetic light-harvesting. *The journal of physical chemistry letters*, 3(4):536–542, 2012.
- [10] Seogjoo J Jang and Benedetta Mennucci. Delocalized excitons in natural light-harvesting complexes. *Reviews of Modern Physics*, 90(3):035003, 2018.
- [11] Sandra Doria, Timothy S Sinclair, Nathan D Klein, Doran IG Bennett, Chern Chuang, Francesca S Freyria, Colby P Steiner, Paolo Foggi, Keith A Nelson, Jianshu Cao, et al. Photochemical control of exciton superradiance in light-harvesting nanotubes. *ACS nano*, 12(5):4556–4564, 2018.
- [12] Francesco Mattiotti, Masaru Kuno, Fausto Borgonovi, Boldizsár Jankó, and G Luca Celardo. Thermal decoherence of superradiance in lead halide perovskite nanocrystal superlattices. *Nano Letters*, 20(10):7382–7388, 2020.
- [13] Francesco Mattiotti, Mohan Sarovar, Giulio G Giusteri, Fausto Borgonovi, and G Luca Celardo. Efficient light harvesting and photon sensing via engineered cooperative effects. *New Journal of Physics*, 24(1):013027, 2022.
- [14] Nicholas Werren, Will Brown, and Erik M Gauger. Light harvesting enhanced by quantum ratchet states. *PRX Energy*, 2(1):013002, 2023.
- [15] Mark Winey and Eileen O’Toole. Centriole structure. *Philosophical Transactions of the Royal Society B: Biological Sciences*, 369(1650):20130457, September 2014.
- [16] Elif Nur Firat-Karalar and Tim Stearns. The centriole duplication cycle. *Philosophical Transactions of the Royal Society B: Biological Sciences*, 369(1650):20130460, 2014.
- [17] Ana Rodrigues-Martins, Maria Riparbelli, Giuliano Callaini, David M Glover, and Monica Bettencourt-Dias. From centriole biogenesis to cellular function: centrioles are essential for cell division at critical developmental stages. *Cell Cycle*, 7(1):11–16, 2008.
- [18] G Albrecht-Buehler. Rudimentary form of cellular “vision”. *Proceedings of the National Academy of Sciences*, 89(17):8288–8292, September 1992.
- [19] Guenter Albrecht-Buehler. Cellular infrared detector appears to be contained in the centrosome. *Cell Motility*, 27(3):262–271, January 1994.
- [20] Guenter Albrecht-Buehler. Autofluorescence of live purple bacteria in the near infrared. *Experimental Cell Research*, 236(1):43–50, October 1997.
- [21] G Albrecht-Buehler. Phagokinetic tracks of 3t3 cells: Parallels between the orientation of track segments and of cellular structures which contain actin or tubulin. *Cell*, 12(2):333–339, October 1977.
- [22] Stephen J Everse. Secondary structure (2°) – beta strands. 2014. [*Online Website*].

- [23] Fridoon J. Ahmad, Yan He, Kenneth A. Myers, Thomas P. Hasaka, Franto Francis, Mark M. Black, and Peter W. Baas. Effects of dynactin disruption and dynein depletion on axonal microtubules. *Traffic*, 7(5):524–537, 2006.
- [24] Paul Matsudaira, Eckhard Mandelkow, Winfried Renner, Lyndal K. Hesterberg, and Klaus Weber. Role of fimbrin and villin in determining the interfilament distances of actin bundles. *Nature*, 301(5897):209–214, January 1983.
- [25] Silvia Pelucchi, Ramona Stringhi, and Elena Marcello. Dendritic spines in alzheimer’s disease: How the actin cytoskeleton contributes to synaptic failure. *International Journal of Molecular Sciences*, 21(3):908, January 2020.
- [26] Linus Pauling, Robert B. Corey, and H. R. Branson. The structure of proteins: Two hydrogen-bonded helical configurations of the polypeptide chain. *Proceedings of the National Academy of Sciences*, 37(4):205–211, April 1951.
- [27] Ben J. Eves, James J. Douth, Ann E. Terry, Han Yin, Martine Moulin, Michael Haertlein, V. Trevor Forsyth, Patrick Flagmeier, Tuomas P. J. Knowles, David M. Dias, Gudrun Lotze, Annela M. Seddon, and Adam M. Squires. Elongation rate and average length of amyloid fibrils in solution using isotope-labelled small-angle neutron scattering. *RSC Chemical Biology*, 2(4):1232–1238, 2021.
- [28] Brandon H. Toyama and Jonathan S. Weissman. Amyloid structure: Conformational diversity and consequences. *Annual Review of Biochemistry*, 80(1):557–585, July 2011.
- [29] I. Segers-Nolten, M. van Raaij, and V. Subramaniam. *Biophysical Analysis of Amyloid Formation*, page 347–359. Elsevier, 2011.
- [30] Mark A. Findeis, Gary M. Musso, Christopher C. Arico-Muendel, Howard W. Benjamin, Arvind M. Hundal, Jung-Ja Lee, Joseph Chin, Michael Kelley, James Wakefield, Neil J. Hayward, and Susan M. Molineaux. Modified-peptide inhibitors of amyloid β -peptide polymerization. *Biochemistry*, 38(21):6791–6800, 1999.
- [31] Rehana Akter, Ping Cao, Harris Noor, Zachary Ridgway, Ling-Hsien Tu, Hui Wang, Amy G. Wong, Xiaoxue Zhang, Andisheh Abedini, Ann Marie Schmidt, and Daniel P. Raleigh. Islet amyloid polypeptide: Structure, function, and pathophysiology. *Journal of Diabetes Research*, 2016:1–18, 2016.
- [32] Robert A. Kyle. Amyloidosis: a convoluted story. *British Journal of Haematology*, 114(3):529–538, 2001.
- [33] Liza Nielsen, Ritu Khurana, Alisa Coats, Sven Frokjaer, Jens Brange, Sandip Vyas, Vladimir N. Uversky, and Anthony L. Fink. Effect of environmental factors on the kinetics of insulin fibril formation: Elucidation of the molecular mechanism. *Biochemistry*, 40(20):6036–6046, 2001. PMID: 11352739.
- [34] Fabrizio Chiti and Christopher M. Dobson. Protein misfolding, amyloid formation, and human disease: A summary of progress over the last decade. *Annual Review of Biochemistry*, 86(1):27–68, June 2017.

- [35] Rebecca Nelson and David Eisenberg. Recent atomic models of amyloid fibril structure. *Current Opinion in Structural Biology*, 16(2):260–265, 2006. Theory and simulation/Macromolecular assemblages.
- [36] J P Brion, D P Hanger, M T Bruce, A M Couck, J Flament-Durand, and B H Anderton. Tau in alzheimer neurofibrillary tangles. n- and c-terminal regions are differentially associated with paired helical filaments and the location of a putative abnormal phosphorylation site. *Biochemical Journal*, 273(1):127–133, January 1991.
- [37] Lester I. Binder, Angela L. Guillozet-Bongaarts, Francisco Garcia-Sierra, and Robert W. Berry. Tau, tangles, and alzheimer’s disease. *Biochimica et Biophysica Acta (BBA) - Molecular Basis of Disease*, 1739(2–3):216–223, January 2005.
- [38] Sian-Yang Ow and Dave E. Dunstan. A brief overview of amyloids and alzheimer’s disease. *Protein Science*, 23(10):1315–1331, July 2014.
- [39] Marco Gulli, Alessia Valzelli, Francesco Mattiotti, Mattia Angeli, Fausto Borgonovi, and Giuseppe Luca Celardo. Macroscopic coherence as an emergent property in molecular nanotubes. *New Journal of Physics*, 21(1):013019, jan 2019.
- [40] Nimrod Moiseyev. *Non-Hermitian Quantum Mechanics*. Cambridge University Press, February 2011.
- [41] Heinz-Peter Breuer and Francesco Petruccione. *The Theory of Open Quantum Systems*. Oxford University PressOxford, January 2007.
- [42] Daniel Manzano. A short introduction to the Lindblad master equation. *AIP Advances*, 10(2):025106, 02 2020.
- [43] G. Lindblad. On the generators of quantum dynamical semigroups. *Communications in Mathematical Physics*, 48(2):119–130, Jun 1976.
- [44] Daniel Havelka, Marco A Deriu, Michal Cifra, and Ondřej Kučera. Deformation pattern in vibrating microtubule: Structural mechanics study based on an atomistic approach. *Scientific Reports*, 7(1):4227, 2017.
- [45] Shunyu Yao and Zhong Wang. Edge states and topological invariants of non-hermitian systems. *Physical Review Letters*, 121(8), August 2018.
- [46] Fei Song, Shunyu Yao, and Zhong Wang. Non-hermitian topological invariants in real space. *Physical Review Letters*, 123(24), December 2019.
- [47] Benjamin Bauer, Rahul Sharma, Majed Chergui, and Malte Oppermann. Exciton decay mechanism in dna single strands: back-electron transfer and ultrafast base motions. *Chemical Science*, 13(18):5230–5242, 2022.
- [48] Nicolas Renaud, Yuri A. Berlin, Frederick D. Lewis, and Mark A. Ratner. Between superexchange and hopping: An intermediate charge-transfer mechanism in poly(a)-poly(t) dna hairpins. *Journal of the American Chemical Society*, 135(10):3953–3963, February 2013.

- [49] Eric R. Bittner. Lattice theory of ultrafast excitonic and charge-transfer dynamics in dna. *The Journal of Chemical Physics*, 125(9), September 2006.
- [50] Vincent A. Spata and Spiridoula Matsika. Role of excitonic coupling and charge-transfer states in the absorption and cd spectra of adenine-based oligonucleotides investigated through qm/mm simulations. *The Journal of Physical Chemistry A*, 118(51):12021–12030, September 2014.
- [51] Kwang Hyok Jong, Yavar T. Azar, Luca Grisanti, Amberley D. Stephens, Saul T. E. Jones, Dan Credgington, Gabriele S. Kaminski Schierle, and Ali Hassanali. Low energy optical excitations as an indicator of structural changes initiated at the termini of amyloid proteins. *Physical Chemistry Chemical Physics*, 21(43):23931–23942, 2019.
- [52] Mark T. Oakley and Jonathan D. Hirst. Charge-transfer transitions in protein circular dichroism calculations. *Journal of the American Chemical Society*, 128(38):12414–12415, September 2006.
- [53] Carlo Andrea Rozzi, Sarah Maria Falke, Nicola Spallanzani, Angel Rubio, Elisa Molinari, Daniele Brida, Margherita Maiuri, Giulio Cerullo, Heiko Schramm, Jens Christoffers, and Christoph Lienau. Quantum coherence controls the charge separation in a prototypical artificial light-harvesting system. *Nature Communications*, 4(1), March 2013.
- [54] A. Asenjo-Garcia, M. Moreno-Cardoner, A. Albrecht, H. J. Kimble, and D. E. Chang. Exponential improvement in photon storage fidelities using subradiance and “selective radiance” in atomic arrays. *Physical Review X*, 7(3), August 2017.
- [55] R. Gutiérrez-Jáuregui and A. Asenjo-Garcia. Directional transport along an atomic chain. *Physical Review A*, 105(4), April 2022.
- [56] H. H. Jen. Phase-imprinted multiphoton subradiant states. *Physical Review A*, 96(2), August 2017.
- [57] Luca Grisanti, Dorothea Pinotsi, Ralph Gebauer, Gabriele S. Kaminski Schierle, and Ali A. Hassanali. A computational study on how structure influences the optical properties in model crystal structures of amyloid fibrils. *Physical Chemistry Chemical Physics*, 19(5):4030–4040, 2017.
- [58] Amberley D. Stephens, Muhammad Nawaz Qaisrani, Michael T. Ruggiero, Gonzalo Díaz Mirón, Uriel N. Morzan, Mariano C. González Lebrero, Saul T. E. Jones, Emiliano Poli, Andrew D. Bond, Philippa J. Woodhams, Elyse M. Kleist, Luca Grisanti, Ralph Gebauer, J. Axel Zeitler, Dan Credgington, Ali Hassanali, and Gabriele S. Kaminski Schierle. Short hydrogen bonds enhance nonaromatic protein-related fluorescence. *Proceedings of the National Academy of Sciences*, 118(21), May 2021.
- [59] Falk Liberta, Sarah Loerch, Matthies Rennegarbe, Angelika Schierhorn, Per Westermark, Gunilla T Westermark, Bouke PC Hazenberg, Nikolaus Grigorieff, Marcus

- Fändrich, and Matthias Schmidt. Cryo-EM fibril structures from systemic AA amyloidosis reveal the species complementarity of pathological amyloids. *Nature communications*, 10(1):1–10, 2019.
- [60] Dong-Hyuk Jang, Jin-Hee Han, Seung-Hee Lee, Yong-Seok Lee, Hyungju Park, Sue-Hyun Lee, Hyoung Kim, and Bong-Kiun Kaang. Cofilin expression induces cofilin-actin rod formation and disrupts synaptic structure and function in aplysia synapses. *Proceedings of the National Academy of Sciences*, 102(44):16072–16077, October 2005.
- [61] James R. Bamberg and Barbara W. Bernstein. Actin dynamics and cofilin-actin rods in alzheimer disease. *Cytoskeleton*, 73(9):477–497, March 2016.
- [62] T. W. Nichols, M. H. Berman, and Jack Tuszynski. Journal of multiscale neuroscience. *Journal of Multiscale Neuroscience*, 2(1):141–158, April 2023.
- [63] Nicolas G. Bazan, Anasheh Halabi, Monica Ertel, and Nicos A. Petasis. Chapter 34 - neuroinflammation. In Scott T. Brady, George J. Siegel, R. Wayne Albers, and Donald L. Price, editors, *Basic Neurochemistry (Eighth Edition)*, pages 610–620. Academic Press, New York, eighth edition edition, 2012.
- [64] P. A. Merz, H. M. Wisniewski, R. A. Somerville, S. A. Bobin, C. L. Masters, and K. Iqbal. Ultrastructural morphology of amyloid fibrils from neuritic and amyloid plaques. *Acta Neuropathologica*, 60(1-2):113–124, 1983.
- [65] Shen Han, Marius Kollmer, Daniel Markx, Stephanie Claus, Paul Walther, and Marcus Fändrich. Amyloid plaque structure and cell surface interactions of β -amyloid fibrils revealed by electron tomography. *Scientific Reports*, 7(1), February 2017.
- [66] Xiang-Qi Mu, Lee Makowski, and Beatrice Magdoff-Fairchild. Analysis of the stability of hemoglobin s double strands. *Biophysical Journal*, 74(1):655–668, January 1998.
- [67] Eric R. Henry, Troy Cellmer, Emily B. Dunkelberger, Belhu Metaferia, James Hofrichter, Quan Li, David Ostrowski, Rodolfo Ghirlando, John M. Louis, Stéphane Moutereau, Frédéric Galactéros, Swee Lay Thein, Pablo Bartolucci, and William A. Eaton. Allosteric control of hemoglobin s fiber formation by oxygen and its relation to the pathophysiology of sickle cell disease. *Proceedings of the National Academy of Sciences*, 117(26):15018–15027, June 2020.
- [68] Travis JA Craddock, Jack A Tuszynski, and Stuart Hameroff. Cytoskeletal signaling: is memory encoded in microtubule lattices by camkii phosphorylation? *PLoS computational biology*, 8(3):e1002421, 2012.
- [69] Travis John Adrian Craddock, Douglas Friesen, Jonathan Mane, Stuart Hameroff, and Jack A Tuszynski. The feasibility of coherent energy transfer in microtubules. *Journal of the Royal Society Interface*, 11(100):20140677, 2014.
- [70] Travis J.A. Craddock, Philip Kurian, Jack A. Tuszynski, and Stuart R. Hameroff. 9 - quantum processes in neurophotonic and the origin of the brain’s spatiotemporal

- hierarchy. In Robert R. Alfano and Lingyan Shi, editors, *Neurophotonics and Biomedical Spectroscopy*, Nanophotonics, pages 189–213. Elsevier, 2019.
- [71] Roger Penrose. *Shadows of the mind*. Oxford University Press, New York, NY, August 1996.
- [72] Jonathan Grad, Griselda Hernandez, and Shaul Mukamel. Radiative decay and energy transfer in molecular aggregates: The role of intermolecular dephasing. *Phys. Rev. A*, 37:3835–3846, May 1988.
- [73] Frank C Spano and Shaul Mukamel. Superradiance in molecular aggregates. *The Journal of Chemical Physics*, 91(2):683–700, 1989.
- [74] T. Bienaimé, R. Bachelard, N. Piovella, and R. Kaiser. Cooperativity in light scattering by cold atoms. *Fortschritte der Physik*, 61(2-3):377–392, 2013.
- [75] Giulio G. Giusteri, Francesco Mattiotti, and G. Luca Celardo. Non-hermitian hamiltonian approach to quantum transport in disordered networks with sinks: Validity and effectiveness. *Phys. Rev. B*, 91:094301, Mar 2015.
- [76] E. Akkermans, A. Gero, and R. Kaiser. Photon localization and dicke superradiance in atomic gases. *Phys. Rev. Lett.*, 101:103602, Sep 2008.
- [77] Jan Löwe, H Li, KH Downing, and E Nogales. Refined structure of α β -tubulin at 3.5 Å resolution. *Journal of molecular biology*, 313(5):1045–1057, 2001.
- [78] S. Schenkl, F. van Mourik, G. van der Zwan, S. Haacke, and M. Chergui. Probing the ultrafast charge translocation of photoexcited retinal in bacteriorhodopsin. *Science*, 309(5736):917–920, August 2005.
- [79] Pinar S Gurel, Laura Y Kim, Paul V Ruijgrok, Tosan Omabegho, Zev Bryant, and Gregory M Alushin. Cryo-em structures reveal specialization at the myosin vi-actin interface and a mechanism of force sensitivity. *Elife*, 6:e31125, 2017.

Supplemental Information

Supplementary Tables and Figures

Figures

We present data that show how mechanical motions in microtubules affect the superradiant states they can support. In Figs. S1 and S2, we display visualizations of superradiant eigenstates obtained by diagonalizing the non-Hermitian Hamiltonian in Eq. 1 in the main text. Each eigenstate is near the lowest excitonic state of the system but is not necessarily the maximally superradiant state. The projection of the eigenstate onto the tryptophan (Trp) site basis gives the probabilities of each Trp being in an excited state. Either monomer chain (α or β) of each tubulin dimer is colored based on the average of the probability of each of the four Trp molecules in that chain being excited. Red implies a higher probability, and blue implies a lower probability. Highly superradiant states in the middle column are delocalized across the microtubule (i.e., a more uniform probability distribution), as reflected in the smaller P_{\max} values shown. (The P_{\min} values for all three columns are all numerically zero, to one part in a trillion.) Each row in Figs. S1 and S2 represents a different (mechanical) vibrational mode, which can be roughly categorized as stretching, bending, torsional, and breathing modes. The three panels in each row represent snapshots of each specific mode at different instances in time. The left and right columns display each mode at their extreme amplitudes of vibration, and the middle column displays each mode at its zero amplitude.

Tables

Table S1 describes how the heatmap colors used for each panel in Figs. S1 and S2 correspond to probability distributions across each microtubule.

Mode	Left Panel		Middle Panel		Right Panel	
	P_{\max}	P_{\min}	P_{\max}	P_{\min}	P_{\max}	P_{\min}
7	0.484	1.73×10^{-17}	0.222	5.74×10^{-15}	0.492	8.95×10^{-16}
8	0.414	1.30×10^{-16}	0.109	1.43×10^{-13}	0.424	5.69×10^{-17}
9	0.499	1.01×10^{-14}	0.218	6.89×10^{-14}	0.498	6.89×10^{-16}
10	0.483	1.24×10^{-16}	0.261	6.78×10^{-16}	0.478	3.70×10^{-17}
11	0.428	3.64×10^{-16}	0.289	1.29×10^{-14}	0.482	7.22×10^{-16}
12	0.499	4.07×10^{-19}	0.290	1.68×10^{-14}	0.499	6.94×10^{-17}
13	0.500	2.09×10^{-16}	0.394	1.05×10^{-15}	0.499	1.98×10^{-17}
14	0.500	1.19×10^{-16}	0.261	2.22×10^{-14}	0.500	5.63×10^{-18}
15	0.481	5.55×10^{-17}	0.126	5.74×10^{-14}	0.358	7.09×10^{-14}
16	0.500	4.13×10^{-18}	0.395	2.92×10^{-15}	0.500	2.72×10^{-17}
17	0.492	6.22×10^{-17}	0.220	4.06×10^{-15}	0.500	2.46×10^{-17}
18	0.498	1.79×10^{-16}	0.303	2.54×10^{-14}	0.490	1.01×10^{-15}
19	0.491	3.39×10^{-16}	0.214	1.745×10^{-15}	0.492	5.10×10^{-16}
20	0.491	2.38×10^{-16}	0.194	2.97×10^{-14}	0.496	1.33×10^{-16}

Table S1: Heatmap ranges for each panel of Figs. S1 and S2. P_{\max} and P_{\min} are the maximum and minimum excitonic occupation probabilities, respectively, which range from 0 to 1. P_{\max} is associated with red, P_{\min} is associated with blue, and intermediate probabilities are associated with green in Figs. S1 and S2.

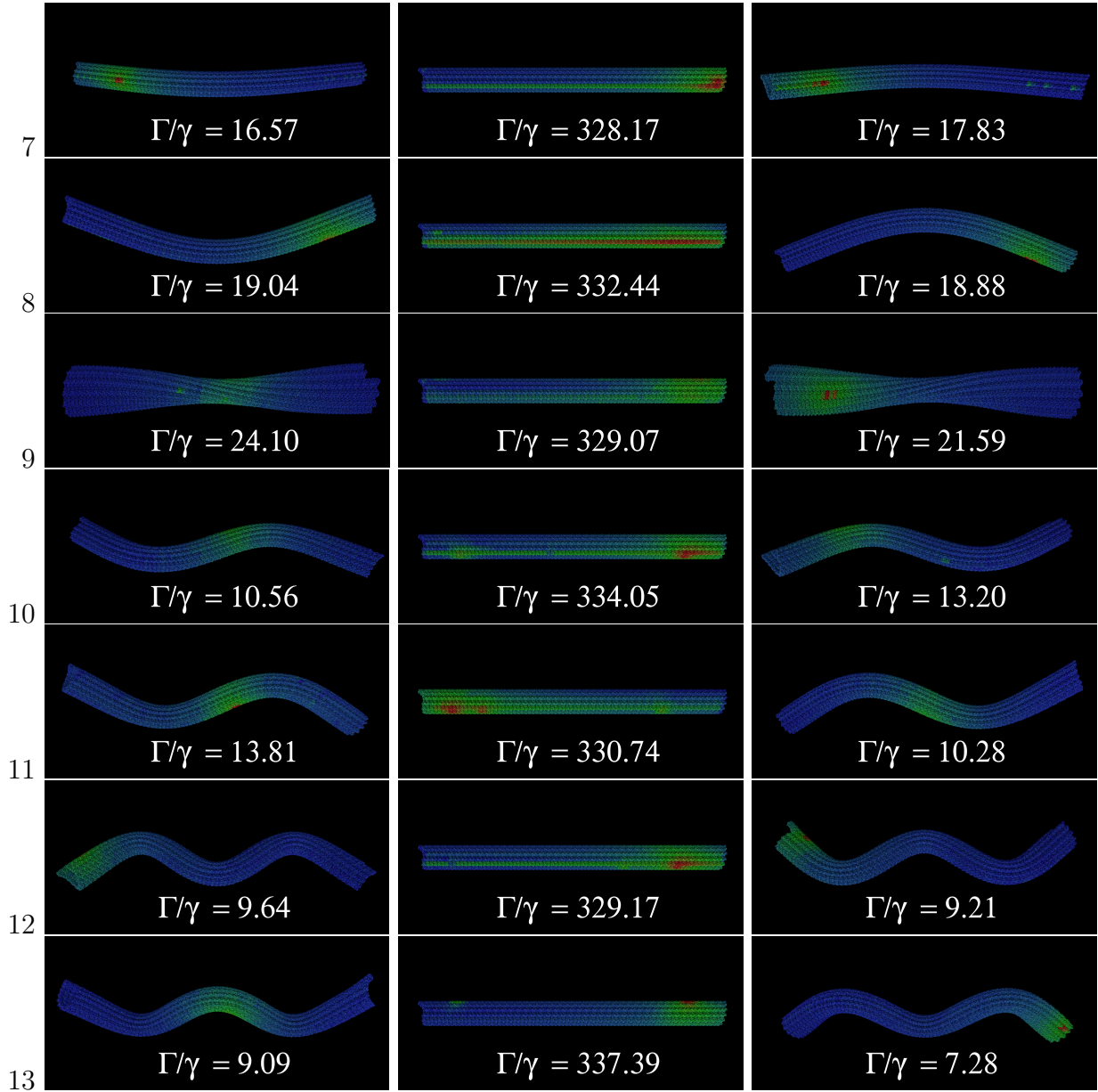


Figure S1: Visualizations of color-coded probability maps showing exciton occupations for low-lying excitonic energy states in the Trp site basis, labeled by maxima of superradiant enhancement factors Γ/γ of Trp networks for deformed (left and right columns) and un-deformed (middle column) microtubules, realized during half a period of each mechanical mode. Atomistic simulations of vibrational motions were realized using the normal mode analyses of entire microtubules obtained from [44]. Each row displays three snapshots of microtubule conformations for each of the vibrational modes 7-13 (e.g., see Fig. 3 of [44]). Rigid modes 1-6 are not shown because they do not involve deformations.

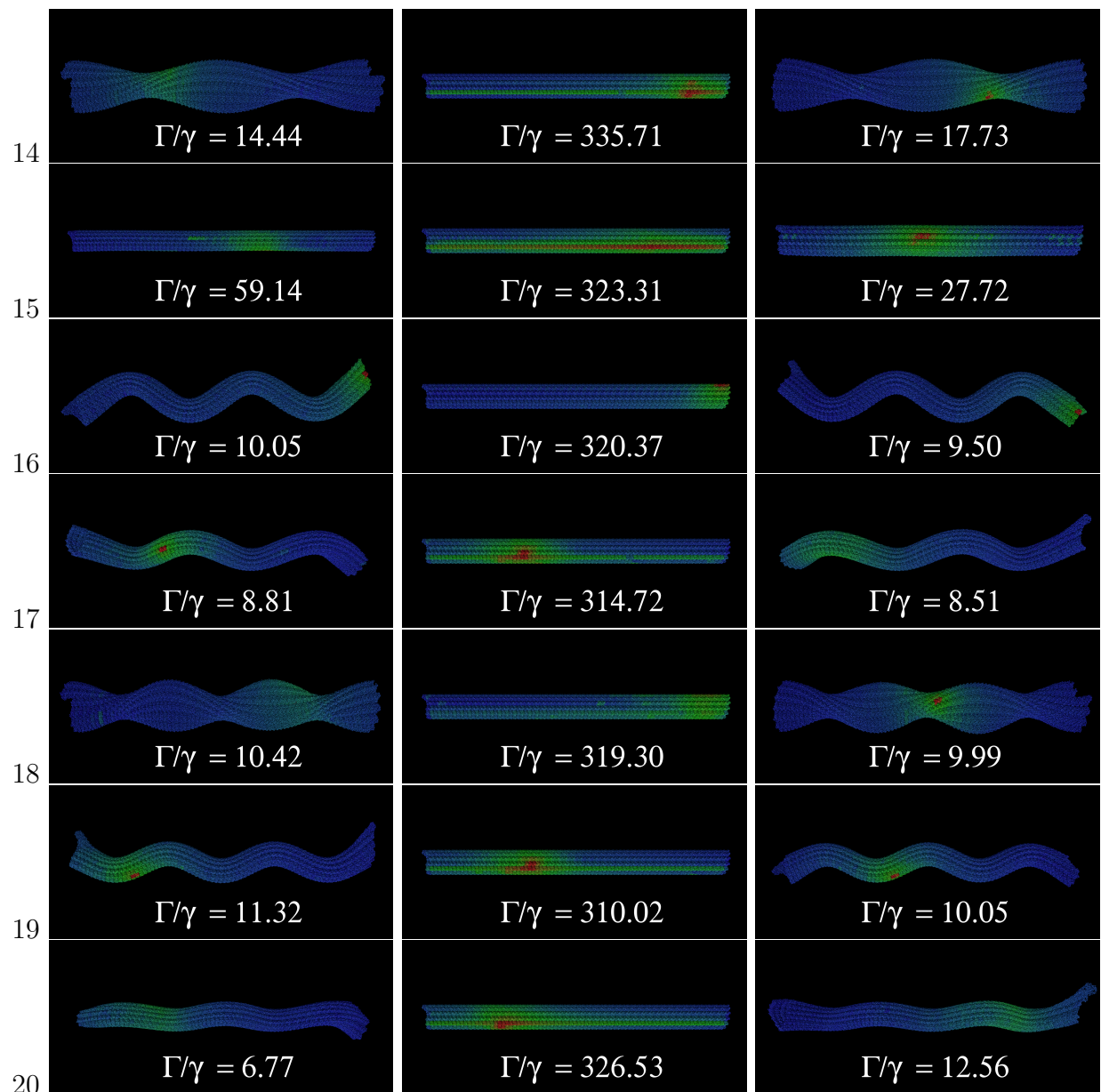


Figure S2: Visualizations of color-coded probability maps showing exciton occupations for low-lying excitonic energy states, labeled by maxima of superradiant enhancement factors Γ/γ of Trp networks for deformed (left and right panels) and undeformed (middle panel) microtubules. Atomistic simulations of vibrational motions were realized using the normal mode analyses of entire microtubules obtained from [44]. Each row displays three snapshots of microtubule conformations for each of the vibrational modes 14-20 (e.g., see Fig. 3 of [44]).